DISCLAIMER

This report was prepared as an account of work sponsored by an agency of the United States Government. Neither the United States Government nor any agency thereof, nor any of their employees, makes any warranty, express or implied, or assumes any legal liability or responsibility for the accuracy, completeness, or usefulness of any information, apparatus, product, or process disclosed, or represents that its use would not infringe privately owned rights. Reference herein to any specific commercial product, process, or service by trade name, trademark, manufacturer, or otherwise does not necessarily constitute or imply its endorsement, recommendation, or favoring by the United States Government or any agency thereof. The views and opinions of authors expressed herein do not necessarily state or reflect those of the United States Government or any agency thereof. Reference herein to any social initiative (including but not limited to Diversity, Equity, and Inclusion (DEI); Community Benefits Plans (CBP); Justice 40; etc.) is made by the Author independent of any current requirement by the United States Government and does not constitute or imply endorsement, recommendation, or support by the United States Government or any agency thereof.

ORNL/TM-2025/4056

Demonstrating Advanced Sensors for In Situ Monitoring Toward Qualification of Nuclear-Relevant Components

Holden C. Hyer
Luke Scime
Zackary Snow
Chase Joslin
Trevor McDonald
Clay Leach
Joshua Kendall
Brandon J. Schreiber
Christian M. Petrie

August 2025

M2CR-22OR0403034

OAK RIDGE
National Laboratory

ORNL IS MANAGED BY UT-BATTELLE LLC FOR THE US DEPARTMENT OF ENERGY

DOCUMENT AVAILABILITY

Online Access: US Department of Energy (DOE) reports produced after 1991 and a growing number of pre-1991 documents are available free via https://www.osti.gov.

The public may also search the National Technical Information Service's National Technical Reports Library (NTRL) for reports not available in digital format.

DOE and DOE contractors should contact DOE's Office of Scientific and Technical Information (OSTI) for reports not currently available in digital format:

US Department of Energy
Office of Scientific and Technical Information
PO Box 62
Oak Ridge, TN 37831-0062
Telephone: (865) 576-8401
Fax: (865) 576-5728
Email: reports@osti.gov
Website: www.osti.gov

This report was prepared as an account of work sponsored by an agency of the United States Government. Neither the United States Government nor any agency thereof, nor any of their employees, makes any warranty, express or implied, or assumes any legal liability or responsibility for the accuracy, completeness, or usefulness of any information, apparatus, product, or process disclosed, or represents that its use would not infringe privately owned rights. Reference herein to any specific commercial product, process, or service by trade name, trademark, manufacturer, or otherwise, does not necessarily constitute or imply its endorsement, recommendation, or favoring by the United States Government or any agency thereof. The views and opinions of authors expressed herein do not necessarily state or reflect those of the United States Government or any agency thereof.

ORNL/TM-2025/4056

Advanced Materials and Manufacturing Technologies Program

DEMONSTRATING ADVANCED SENSORS FOR IN SITU MONITORING TOWARD QUALIFICATION OF NUCLEAR-RELEVANT COMPONENTS

Holden C. Hyer
Luke Scime
Zackary Snow
Chase Joslin
Trevor McDonald
Clay Leach
Joshua Kendall
Brandon J. Schreiber
Christian M. Petrie

August 2025

Milestone #: M2CR-22OR0403034

Prepared by
OAK RIDGE NATIONAL LABORATORY
Oak Ridge, TN 37831
managed by
UT-BATTELLE LLC
for the
US DEPARTMENT OF ENERGY
under contract DE-AC05-00OR22725

CONTENTS

LIST OF FIGURES

LIST OF TABLES

ABBREVIATIONS

AI	artificial intelligence
AM	additive manufacturing
AMMT	Advanced Materials and Manufacturing Technologies
ART	Advanced Reactors Technologies
ASME	American Society of Mechanical Engineers
BPVC	Boiler and Pressure Vessel Code
CNN	convoluted neural network
DED	direct energy deposition
DMSCNN	dynamic multilabel segmentation convolutional neural network
DOE	US Department of Energy
fps	frames per second
HFIR	High Flux Isotope Reactor
IN617	Inconel 617
LPBF	laser powder bed fusion
LWIR	long-wavelength infrared
MDF	Manufacturing Demonstration Facility
NE	Office of Nuclear Energy
NIR	near-infrared
ORNL	Oak Ridge National Laboratory
PM-HIP	powder metallurgy hot isostatic pressing
SS	stainless steel
TCR	Transformational Challenge Reactor
UI	user interface
VED	volumetric energy density
VPPM	voxel property prediction model
XCT	X-ray computed tomography

EXECUTIVE SUMMARY

The U.S. Department of Energy's Office of Nuclear Energy Advanced Materials and Manufacturing Technologies (AMMT) program is pursuing qualification of laser powder bed fusion (LPBF) components for nuclear applications. A major focus of this effort is the use of in situ process monitoring and machine learning–based tools to establish real-time quality assurance. The primary objective of this report is to identify and evaluate the most relevant in situ sensor systems for LPBF, and to document the deployment of these systems across platforms critical to the AMMT program. This work demonstrates how in situ monitoring can detect process anomalies, track geometry-dependent flaws, and identify limiting combinations of processing parameters—particularly those related to energy density and complex geometries (e.g., overhanging structures). To support this goal, a diverse suite of sensor modalities was evaluated across LPBF platforms, including visible and near-infrared (NIR) imaging, fringe projection profilometry, long-wavelength infrared (LWIR) thermography, and high-speed photodiode/pyrometry systems. These sensor streams were integrated with Peregrine, a machine-agnostic software platform that, among other capabilities, can generate real-time process anomaly classification. This report documents sensor deployments on multiple AMMT flagship platforms, including the Concept Laser M2 and Renishaw AM400/AM250 systems. Calibration builds with complex, flaw-prone geometries such as unsupported overhangs, stepped features, and thin walls, were used to evaluate how well Peregrine and its associated sensors could detect process anomalies and other instabilities under varied energy densities. It will be shown how Peregrine reliably identifies common process anomalies such as recoater streaking, superelevation, etc., and can be used in post-build analysis for anomaly spatial distributions throughout the build height to better understand the impact of geometry and processing parameter choice on the build. This work demonstrates measurable progress toward the vision that components can be *born-qualified* by establishing a real-time monitoring framework, identifying limiting process conditions, and laying the foundation for sensor fusion–enabled prediction pipelines that are scalable across platforms and applicable to nuclear-relevant components.

1. INTRODUCTION

1.1 THE MATERIALS QUALIFICATION CHALLENGE

Many of the materials used in the construction of the first commercial nuclear reactors back in the 1950s included zirconium alloys for fuel cladding; stainless steels (SSs) for structural components, including the pressure vessel; and some nickel-based superalloys in coolant pumps or electricity-generating steam turbines [1-3]. Despite significant advances in alloy development over the past 70 years, advanced reactor concepts must continue to use components designed based on these decades-old material systems since little headway has been made in qualifying new alloy systems. Qualification of structural materials for nuclear applications has long been a time- and resource-intensive challenge. The American Society of Mechanical Engineers (ASME) *Boiler and Pressure Vessel Code* (BPVC), for example, requires exhaustive mechanical testing (e.g., tensile, creep, fatigue) to assess material performance. In some cases, the Nuclear Regulatory Commission requires long-term irradiation exposure data to accompany radiation effects on said mechanical performance. Sections I and VIII of the BPVC have an approximately 10 year life requirement based on an extrapolated 100,000 h creep rupture lifetime. However, the more rigorous Section III, Division 5, addresses design lifetimes approaching 60 years, following an extrapolated 500,000 h creep rupture requirement.

A number of alloy systems have been approved under Sections I and VIII, including a range of ferritic and austenitic carbon steels, as well as copper- and aluminum-based systems. With only a 10-year design life, these alloys are typically restricted to non-load-bearing components or those that experience little to no irradiation dose. As a result, more consequential components—such as the reactor pressure vessel—must be fabricated from Section III alloys, which are currently limited to six systems: SS316, SS304, Grade 91 (9Cr–1Mo–V), Grade 22 (2.25Cr–1Mo), 800H, and Inconel 617 (IN617). Alloy IN617 is the most recent addition; it became fully qualified and incorporated into the BPVC in 2020. For context, a code case for IN617 was first drafted in the early 1990s but was not approved for execution until 2001 [4]. A code case for alloy 709, initiated in 2014 under the Advanced Reactors Technologies (ART) program of the US Department of Energy (DOE) Office of Nuclear Energy (NE), is currently in progress to meet the Section III design life of 500,000 h, but full qualification could still take another 5+ years [5, 6].

Conventional approaches to materials qualification typically follow a design–manufacture–test workflow, requiring extensive iteration time with no internal feedback loop in the process [7-9]. Circumventing iterative learning to shorten the timeline to qualification is unlikely to be adopted in industries such as nuclear energy that have numerous stakeholders ranging from investors to the general public. The deployment of advanced manufacturing techniques such as additive manufacturing (AM) has gained traction because of increased design freedom and the ability to fabricate complex components. Modeling-informed geometric optimization can now be performed early in the design process without the constraints of conventional manufacturing and without the need for iterative prototyping [9, 10]. For example, the DOE NE Transformational Challenge Reactor (TCR) program sought to leverage the inherent flexibility of AM to assemble and build an advanced reactor with high modularity, site-specific monitoring, and passive safety features not found in conventional light-water reactors [9, 11]. The TCR program demonstrated the feasibility of designing, fabricating, and evaluating components for nuclear application, all within a single week [12, 13].

The TCR approach took a more manufacturing- and microstructure-informed path toward qualification, allowing for immediate feedback into modeling efforts to iterate on component design [9, 10]. To build on that framework and establish a broader rapid qualification network, DOE NE launched the Advanced Materials and Manufacturing Technologies (AMMT) program, with a focus on evaluating advanced manufacturing processes for the nuclear energy application. Since its inception in 2023, the AMMT program has identified laser powder bed fusion (LPBF), wire-arc and blown-powder direct energy deposition (DED), and powder metallurgy hot isostatic pressing (PM-HIP) as the most diverse and applicable technologies for the nuclear sector [14]. Particular focus has been placed on LPBF because of its ability to realize fine geometric features (>100 µm) and the extensive body of existing work already available on Section III alloys such as SS316 and SS304 processed by AM processes [14].

A large body of work has investigated LPBF for processing multiple commercial alloys and employing in situ monitoring to understand the process on macro and micro levels. The AMMT program seeks to establish a qualification framework using in situ monitoring during LPBF as a core element to the framework, as visualized in Figure 1. Large swaths of data can be recorded in situ and uploaded to a digital thread for said component that contains all its relevant information cradle to grave, from the powder feedstock used to create the component to all characterization performed postbuild, to any data regarding its performance in application. Ultimately, in situ monitoring would become a real-time analysis tool that determines the manufacturing quality that meets the desired specification and is born-qualified upon manufacturing completion (which could include thermomechanical processing following AM), allowing for immediate application.

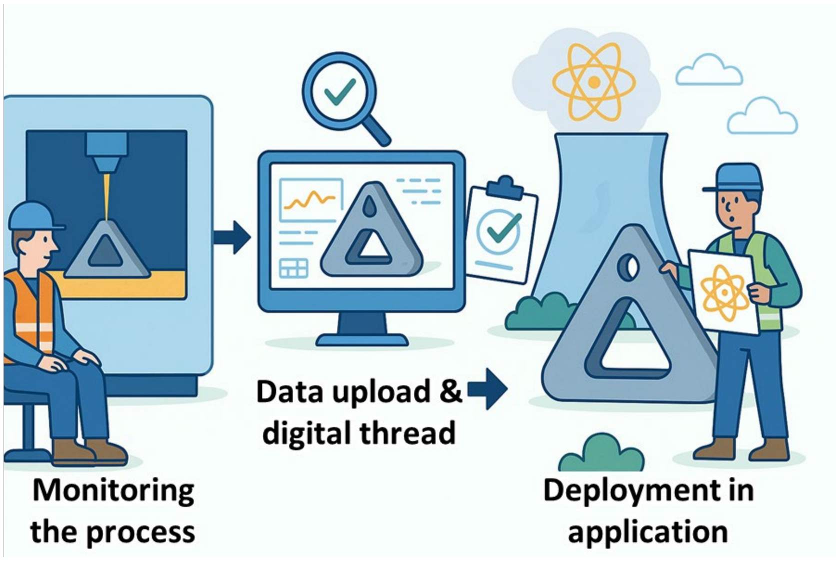

Figure 1. Following a born-qualified approach toward manufacturing components for the nuclear industry.

1.2 COMPLEXITIES OF LPBF

LPBF involves the selective laser melting of a powder bed, additively building material layer by layer [15]. Dialing the processing parameters to fabricate *optimized* material—often considered to be dense with minimal voids and a near-isotropic microstructure and mechanical responses that are near isotropic [15]—can be difficult to achieve. Many different user-defined processing parameters can be varied in an LPBF system; the most common include the laser power; laser spot size; raster scan speed of the laser; distance between consecutive scans, known as the *hatch spacing*; or the powder layer thickness [15]. Operators and developers try to normalize the energy input into the system through energy density. An industry standard is the volumetric energy density (VED), defined in Eq. (1) [15]:

$$VED = \frac{P}{V \times HS \times LT}, \tag{1}$$

where P is the laser power, V is raster velocity, HS is the hatch spacing, and LT is the powder layer thickness [16]. For pulsed laser systems such as those used in this report, the velocity is defined by Eq. (2):

$$V = \frac{PD}{DT+OT}, \tag{2}$$

where PD is the distance between consecutive points that the laser hops (i.e., point distance), DT is the dwell time at each point, and OT is the dead time, during which the laser is off, i.e., no power output [16].

LPBF is host to some of the highest cooling rates in any bulk manufacturing process, often reaching magnitudes of 10^5–10^7 K/s [16, 17]. Variations in energy density can greatly influence the thermal history of the printed component, often finding that larger energy densities lower the cooling rate (retention of heat) and smaller energy densities have higher cooling rates (faster heat dissipation) [16, 17]. Process mapping is often performed to identify a process window(s) in which the desired alloy can be printed to the *optimized* condition. Figure 2 shows an example of different regimes of voids and flaws identified in LPBF-processed SS316L [16]: at lower energy densities, irregular pore formation occurs from lack of fusion due to insufficient melting and interparticle joining. Eventually, near-full-density material can be achieved at some intermediate energy density. Continuing to increase the energy density past the intermediate value starts to cause such intense vaporization that keyholes form, penetrating into the base and often entrapping gas, leaving behind more circular porosity.

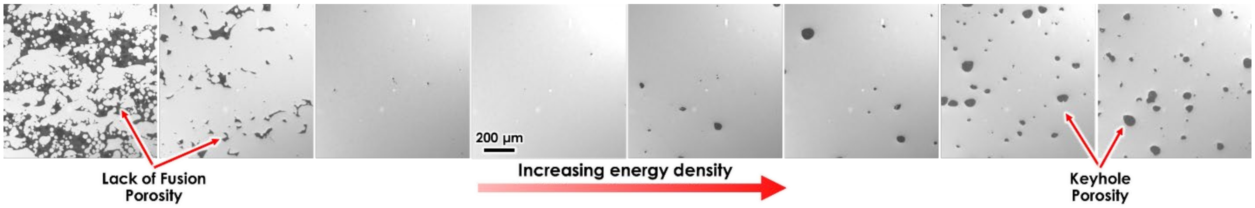

Figure 2. Optical images of SS316L processed with different energy densities [16].

Even with identification of a processing window in which material can be printed with minimal voids, either lack of fusion or keyhole type porosity, and without any detrimental defects or cracks, further optimization is required to identify the desired microstructure and its resulting mechanical performance. Figure 3 shows grain maps collected using electron backscatter diffraction for the austenite phase of SS316L for samples fabricated with LPBF using different energy densities that all yielded >99% dense material, albeit, with some differences in small-scale flaw formation. As shown from the images, density optimization is only the first step. The grain structures in Figure 3 often vary in grain size and texture but generally show a columnar microstructure. Although efforts have been reported to fabricate material with a more refined and/or equiaxed grain structure by more precise control of the laser scan strategy [18], heterogenous microstructures are often observed. Repetitive local laser melting can result in epitaxial grain growth through multiple layers that builds the columnar grain structures. Moreover, the rapid solidification is conducive to solute segregation that may form dendritic/cellular subgrain structures within the material [19]. These differences in grain structure can greatly influence the mechanical properties, particularly with a directional dependence parallel vs. perpendicular to the build direction [19-21].

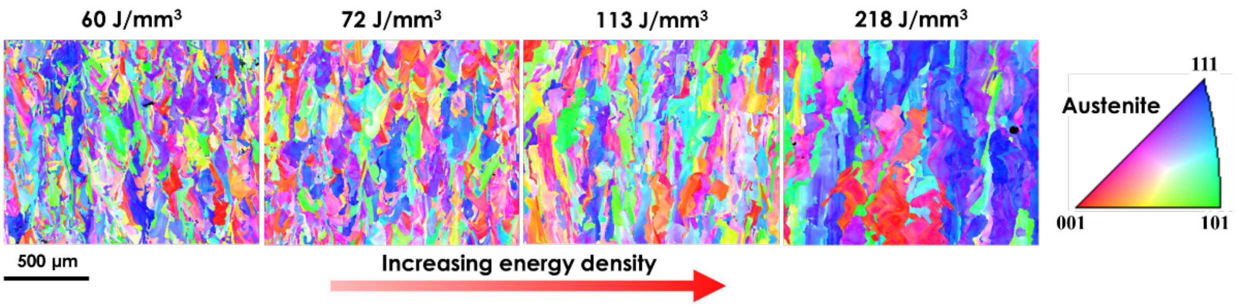

Figure 3. Electron backscatter diffraction grain maps for LPBF-fabricated SS316L at different energy densities. Small changes to thermal history can dramatically influence material performance [18]. As such, the AMMT program has prioritized process optimization efforts for nuclear-relevant alloys, with SS316H serving as a flagship system [14, 22]. The approach involves defining a broad parameter space, as shown in Figure 4(a), and varying energy densities and scan strategies across a statistically designed (i.e., employing a design of experiments) set of builds [23-25]. These builds are often composed of simple geometries such as cubes or cylinders, which can then be easily characterized using microscopy, porosity analysis, and mechanical testing [23-25]. Downselection from this broader process map can help isolate parameter sets that yield the desired material behavior.

The main challenge with process mapping studies is that bulk and simple geometries do not always reflect the complexity of features that might be found in actual components. Features such as thin walls or overhangs pose challenges because of the lack of consistent heat conduction paths [26], as demonstrated in Figure 4(b). Heat can be conducted in a radial manner in bulk structures, as shown in Figure 4(b), with a direct downward path to the build plate. Building thin walls may have a path downward for heat to conduct, but over time, a small amount of material is available for heat conduction because the wall starts to become insulated by the powder bed and there is no additional material is the radial direction, as demonstrated in Figure 4(b). Similarly, structures that overhang away from the bulk structure rest on a thermally insulating powder bed, requiring heat to conduct through the only solid path, as shown in Figure 4(b). These variations in the local cooling rate affect the thermal gradients and residual stress evolution in ways not captured by cube-based optimization studies Any path for heat conduction may appear to be sufficient, but the more time the heat stays in the material, the higher potential for residual stress evolution over time, which can cause warpage, cracking, or delamination between layers [15, 27]. Therefore, some uncertainty still exists in translating what is learned at the process optimization stage to actual fabrication of components.

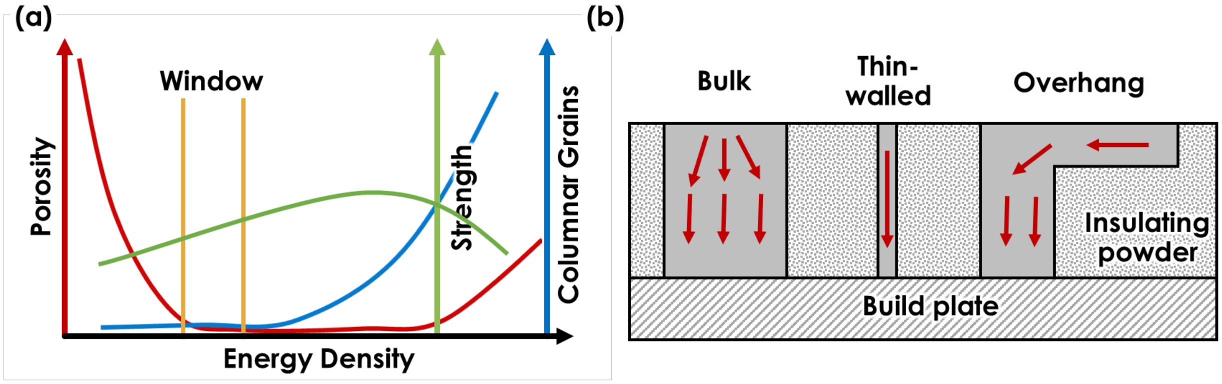

Figure 4. (a) Generalized LPBF process optimization window identification based on characterization of material as a function of energy density; the idea being to map out the area of minimum porosity, and further down select the process window based on other requirements such as the microstructure or mechanical response. (b) Heat conduction paths for various geometric types at perceived in the powder bed during printing; bulk geometries have material to conduct radially, whereas the thin walled structures have only a single path of conduction as they are insulated on both sides; the overhang structures must conduct heat through the only solid bridge to the bulk, which is not a direct path of heat conduction and can result in heat retention for long durations.

Reducing the uncertainty in microstructure and properties of components fabricated from LPBF is critical for quality assurance and establishing a qualification framework that is expected to be adopted by industry. In situ process monitoring can be implemented to identify any potential process anomalies or changes in thermal history during a build that may be outside of the expected window of optimization [28]. The current state of the art for in situ monitoring often includes taking visible or near-infrared (NIR) camera images before, during, and after the laser melting; pixels are then classified into process anomalies using computer vision and machine learning algorithms, such as convolutional neural networks (CNNs) to train the artificial intelligence (AI) models [29-33]. Process anomalies include unexpected or undesired occurrences such as recoater streaking, condensate buildup, or superelevation above the build plane. Process anomalies could lead to flaws or limiting defects within the component that may become detrimental to the component's performance. However, the relationship between the observed process anomalies and the impact of the component macro- or microstructure is not quite clear, although, some correlations have been made [33]. Other sensors could potentially be included during in situ monitoring to provide additional information that may help better train the CNN and even move toward predicting any limiting defect formation, microstructure features, and the resulting mechanical performance.

To improve this linkage, additional sensors can be integrated during printing. For example, thermal sensors or spectrometers capable of measuring high-speed radiative emission may help quantify the melt pool temperature and cooling rate—two parameters closely tied to microstructure and stress evolution. Traditional NIR sampling is done slowly enough to resolve with spatial and temporal resolution (i.e., a voxel size that provides enough data points on finer features >200 µm that don't end up blending with the background) across the entire powder bed, making it difficult to resolve the rapid thermal kinetics in LPBF. High-speed CCD cameras or pyrometers operating at broader wavelength ranges offer a potential path forward by capturing thermal data on submillisecond timescales [34]; however, they suffer from limited fields of view or cumbersome amounts of data.

At Oak Ridge National Laboratory (ORNL), the Manufacturing Demonstration Facility (MDF) has developed the Peregrine software suite to manage and analyze in situ sensor data [31-33, 35]. Peregrine serves as a digital framework that collects synchronized data from process monitoring sensors (e.g., cameras, thermocouples, etc.), processes this information through a deep learning algorithm for real-time anomaly classification, and offers tools for visualizing build history postprocess [31-33, 35]. Importantly, Peregrine is designed to accommodate new sensor inputs and analytical tools, enabling it to evolve alongside monitoring technologies. Using Peregrine or similar software would be the driver toward qualification.

Figure 5 shows a hypothetical complex component, such as an open-porous structure found in heat exchangers for advanced reactor concepts, which is being fabricated with LPBF. In situ sensors may measure a *hot spot* (colloquially reference for this purposes of this report to describe a high probability region where something is off ideal condition) that is immediately identified as a process anomaly within Peregrine or similar software. Ostensibly, the digital twin would feed through a CNN-based AI that has been trained on a significant amount of ground truth postbuild characterization results about relevant components from the same material. The AI would be able to determine if the resulting microstructure in the hot spot region is something desired (homogenous grains) or something less desirable (heterogenous grains), as well as how that might affect the mechanical performance.

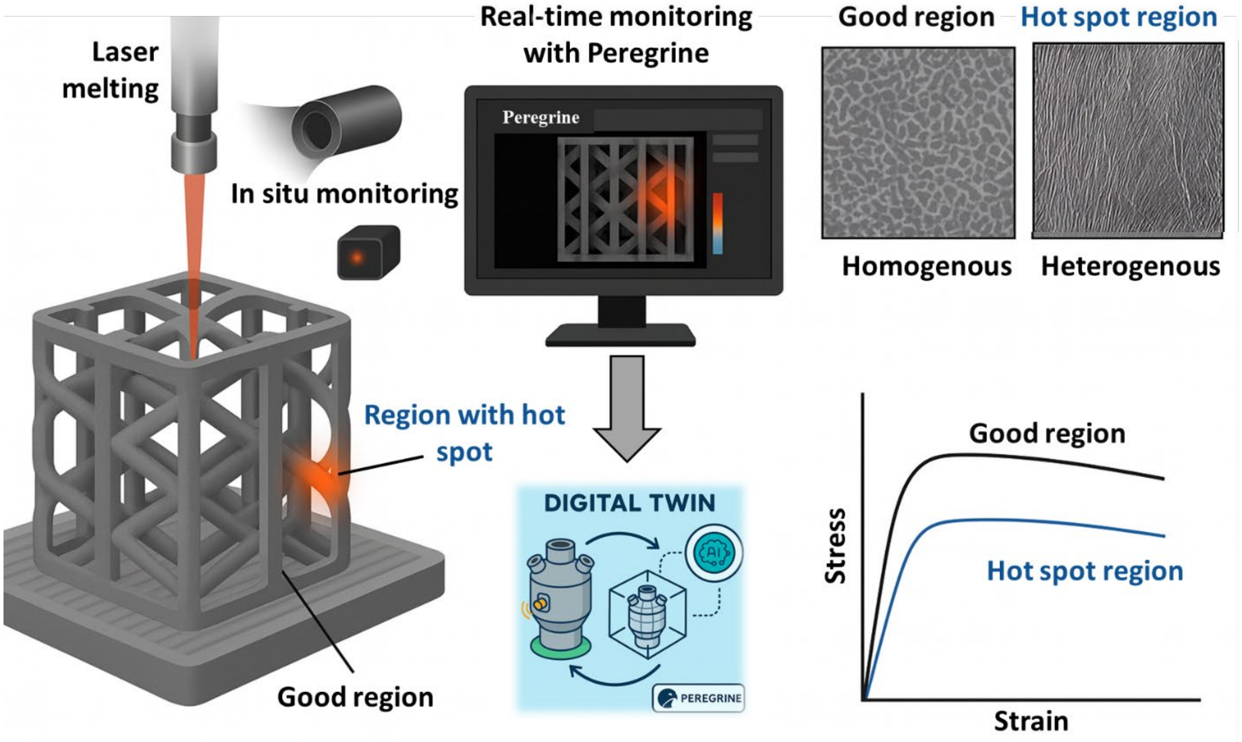

Figure 5. Demonstration of using Peregrine and in situ monitoring as a qualification tool. A hypothetical representation showing, first, in situ monitoring with various sensors is able to detect a hot spot identified as a process anomaly in Peregrine. Based on characterization data from optimization studies, Peregrine would use AI and a digital twin on the component to determine quantities such as the expected grain structure and resulting mechanical properties in the region of the hot spot, ultimately providing quality assurance on the spot.

This report highlights various in situ monitoring strategies for LPBF that were developed and/or evaluated under the AMMT program. It focuses on integrating sensing technologies with data analytics to enhance process understanding, support real-time quality assurance, and contribute to a broader framework for qualifying AM components for nuclear energy applications. This report provides a general overview of how various state-of-the-art sensors are being used in LPBF, the specific ways that the data from these sensors are used in identification of process anomalies, and an evaluation of newly deployed sensor suites under the AMMT program.

2. SENSORS FOR IN SITU PROCESS MONITORING

Figure 6 shows a generalized family tree of different sensor types that can be used for in situ monitoring of LPBF. Starting at the bottom of the tree, the most obvious sensors include probe types that could be used to monitor machine vitals: oxygen levels, temperature of the build chamber systems or optics column, pressure, inlet/outlet flow rate, and more. Probe sensors are typically used to monitor the machine itself but could indicate problems such as an air leak letting an excess of oxygen into the chamber or overheating in the optic galvo mirror that may cause damage to the laser functionality. Other than the LPBF processing parameters, other environmental conditions can also induce changes during the print, and probe sensors can be used to monitor these subsystems [36].

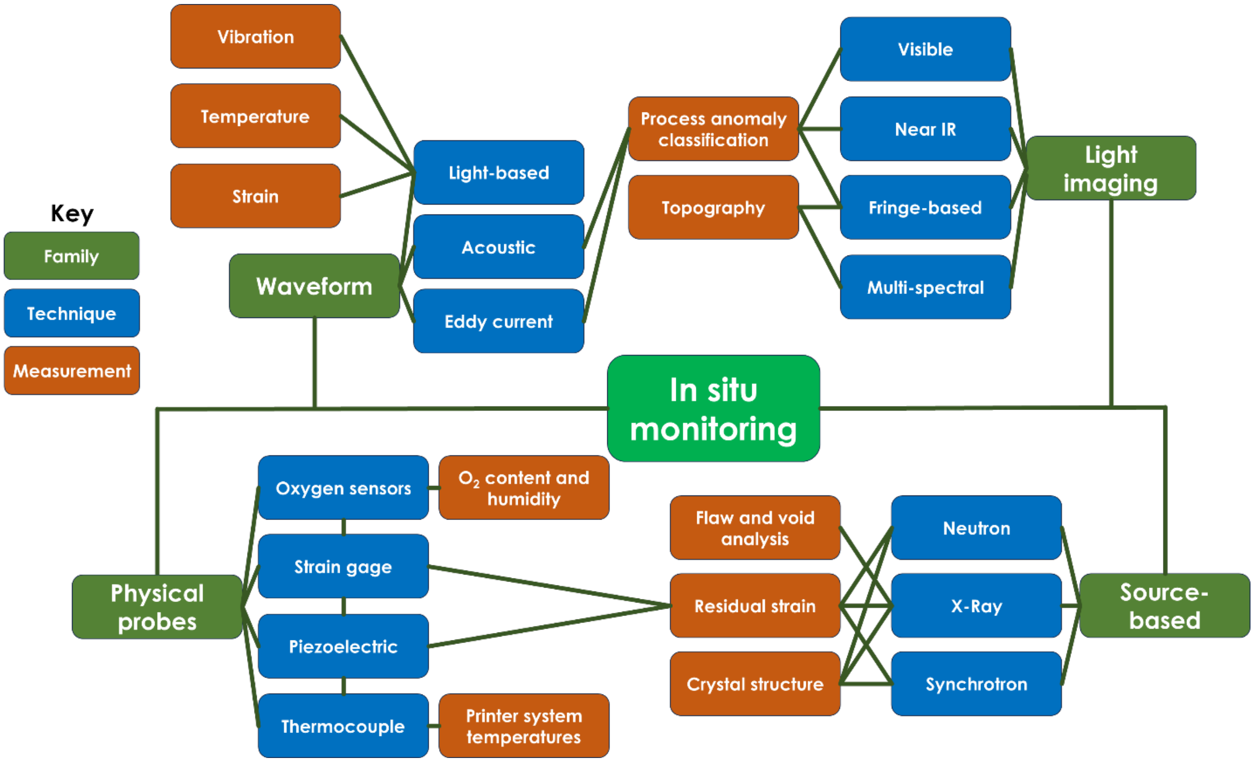

Figure 6. Family tree for sensor types deployable for in situ monitoring in LPBF.

Laser melting of the powder bed is chaotic, and powder particles—some of which may be hot enough to attract any remaining oxygen species—are ejected into all directions in the build chamber [37]. Most commercial LPBF systems use a gas recirculation pump to flow an argon shroud over the top of the powder bed in an effort to capture these eject power particles and transport them to the side of the build plate. The gas recirculation pump is often in line with a filter that captures the fine particles swept in the gas flow, and a filling filter can affect the back pressure into the build chamber. The back pressure and flow rate of the gas recirculation pump, as well as the distribution of the gas into a plane-like movement parallel to the build plane, can affect the outcome of the printing. Continuous monitoring of the recirculation pump using probe-type sensors gives the operators the necessary machine vitals to ensure that the same or desired flow is in check.

Other types of probe sensors such as strain gauges, piezoelectrics, or fiber optics could be used to monitor residual stress that may indicate deleterious cracking, warpage, or delamination. These strain sensors could be directly embedded in the build plate or mounting plate to measure the evolved residual stress over the build height [38, 39]. In a similar vein, acoustic accelerometers may be able to monitor acoustic emissions from cracks and/or the vibrational modes of the system, relying on connections to the recirculation pump to provide the acoustic excitation. Cracking or other major events would likely result in a shift or broadening of the acoustic profile, providing a rapid-response mechanism that could trigger a pause or build stoppage.

Beyond passive sensing, source-based methods such as neutron diffraction, synchrotron radiation, and X-ray imaging offer deeper insight into residual stress and phase evolution. However, it is difficult and costly to maintain these types of sources, making it infeasible to deploy these types of systems in commercial LPBF printers. Neutron and synchrotron sources in particular require large amounts of energy and are usually only found at national laboratories. X-ray sources are easier to deploy in a condensed form but would require significant design alteration and strategizing toward manufacturing an LPBF printer on a mass scale. High-speed, in situ X-ray imaging and diffraction have been performed on small-scale LPBF setups [10, 40-42] but are used mostly to observe and analyze melting modes. Sources are more applicable for ex situ characterization postbuild. Characterization could be performed during the process optimization stage or for random screening for quality assurance purposes. X-ray computed tomography (XCT) in particular can be used to identify voids in component postprinting [43].

As mentioned earlier, the most promising candidates for real-time quality assurance lie in optical and waveform-based techniques [44]. Multi-modal imaging systems, which pair visible and NIR cameras, are considered the current state of the art for in situ monitoring [44]. Visible cameras are used to track surface morphology, and NIR cameras provide thermal emission data during laser melting. Combined, these image stacks can be processed through machine learning algorithms trained to classify various process anomalies. These include defects such as spatter, swelling, recoater streaking, or superelevation above the intended build plane [31]. The details of these imaging systems and their current implementation under the AMMT program are discussed in the following section.

Further enhancement to imaging-based monitoring can be achieved through techniques such as fringe projection [45-49] or multispectral lighting [50, 51]. In fringe projection, a light pattern with a sinusoidal intensity is cast onto the powder bed surface. Any surface perturbations will distort the projected fringe, and by comparing the captured pattern to the expected (ideal) profile, a layer-specific topographic map can be reconstructed [45, 46]. Repeating this process across all layers allows for full 3D reconstruction of the component during the build, enabling identification of internal voids or unexpected height variations. Multispectral lighting works on a similar principle but uses light of multiple wavelengths to interrogate the powder bed surface. Variations in surface reflectivity across different spectra are used to construct a profile of surface roughness [50, 51], analogous to the fringe technique. These methods have shown promise for tracking geometry evolutions in situ and could eventually serve as complementary data streams for enhancing CNN training or postprocessing analysis pipelines.

3. CURRENT STATE OF THE ART

This section details the currently applied sensor suite to LPBF systems at MDF, implementation of Peregrine for in situ monitoring, and efforts into identifying process anomalies. Recent advances in sensor improvement and updates to the Peregrine user interface (UI) are discussed. Data from so-called calibration builds are also presented from two machines: (1) the M2 Concept Laser system, which is currently the flagship LPBF system of the AMMT program, and (2) a Renishaw AM400, which both Argonne National Laboratory and ORNL have in common for cross-lab comparison between builds.

3.1 REAL-TIME-BASED MONITORING WITH PEREGRINE

The dual visible + NIR camera setup has been deployed across several LPBF systems at MDF, including the Renishaw AM400 and M2 Concept Laser. Figure 7(a) shows how these cameras are mounted inside the build chambers to capture as much of the build area as possible. Between built-in and after-market LEDs and adjusted camera exposure settings, the lighting is tuned to reduce surface reflections and still maintain enough contrast to resolve topographic features across the powder bed.

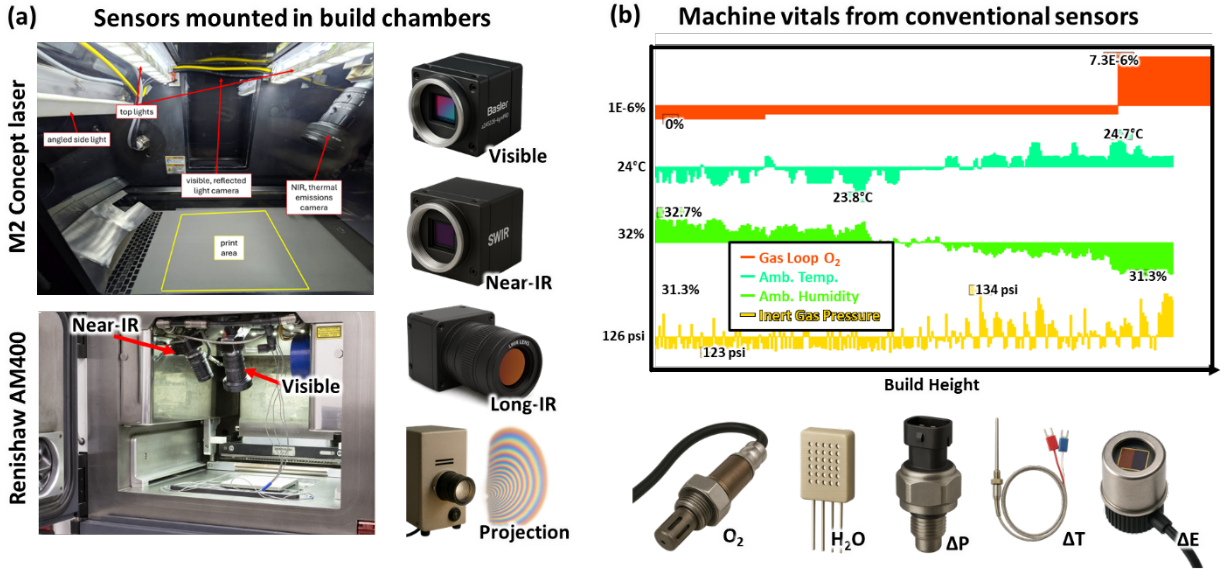

Figure 7. (a) Mounting of cameras inside the M2 Concept Laser and Renishaw AM400 build chambers; various camera types that are being deployed across LPBF machines at ORNL. (b) Sampled machine vitals during a build, including the O_2 level with the gas circulation loop, ambient temperature and humidity inside the build chamber, and the pressure in the inert gas line to the machine. Various probe-type sensors can be found in commercial printers, including those for changes in O_2, humidity (H_2O), pressure (ΔP), temperature (ΔT), and radiative emission (ΔE) from the laser melting.

In addition to the camera systems, most LPBF machines are equipped with multiple probe-type sensors to monitor machine vitals during the build. Figure 7(b) shows a set of sampled data from the M2 system, including chamber O_2 levels, temperature, pressure, and humidity. The M2 includes a ZrO_2 sensor for oxygen detection in the recirculating gas line, a dielectric humidity sensor (H_2O), pressure transducers for the inert gas loop (ΔP), thermocouples to measure thermal drift (ΔT) inside the build chamber and optics column, and a photodiode for detecting radiative emissions (ΔE) during melting. As mentioned earlier, factors beyond processing parameters can influence component quality. These probe sensors provide a baseline for checking system stability. A rise in O_2 or H_2O could indicate a leak in the chamber. A shift in ΔT might suggest overheating of internal optics. Changes in ΔP could reflect a blockage or instability in the gas recirculation loop. These signals, taken together with the image data from the camera systems, feed into the digital thread framework for tracking changes in the print environment and identifying potential anomalies in real time.

The dual-camera system collects visible and NIR images at multiple time points per layer during a build, typically after the laser melting step and recoater passes. The NIR camera captures thermal emissions at a frame rate of approximately 2–5 frames per second (fps) during melting, producing a short video buffer per layer. Figure 8(a) shows a comparison between older and more recent image data captured over the past 1.5 years. Improvements to hardware and image processing workflows have reduced camera artifacts, particularly in the NIR images, and increased the level of detail that can be resolved. In the visible spectrum, adjustments to lighting and exposure have improved contrast and surface topography detection, especially in postspread frames, in which small irregularities can be difficult to distinguish.

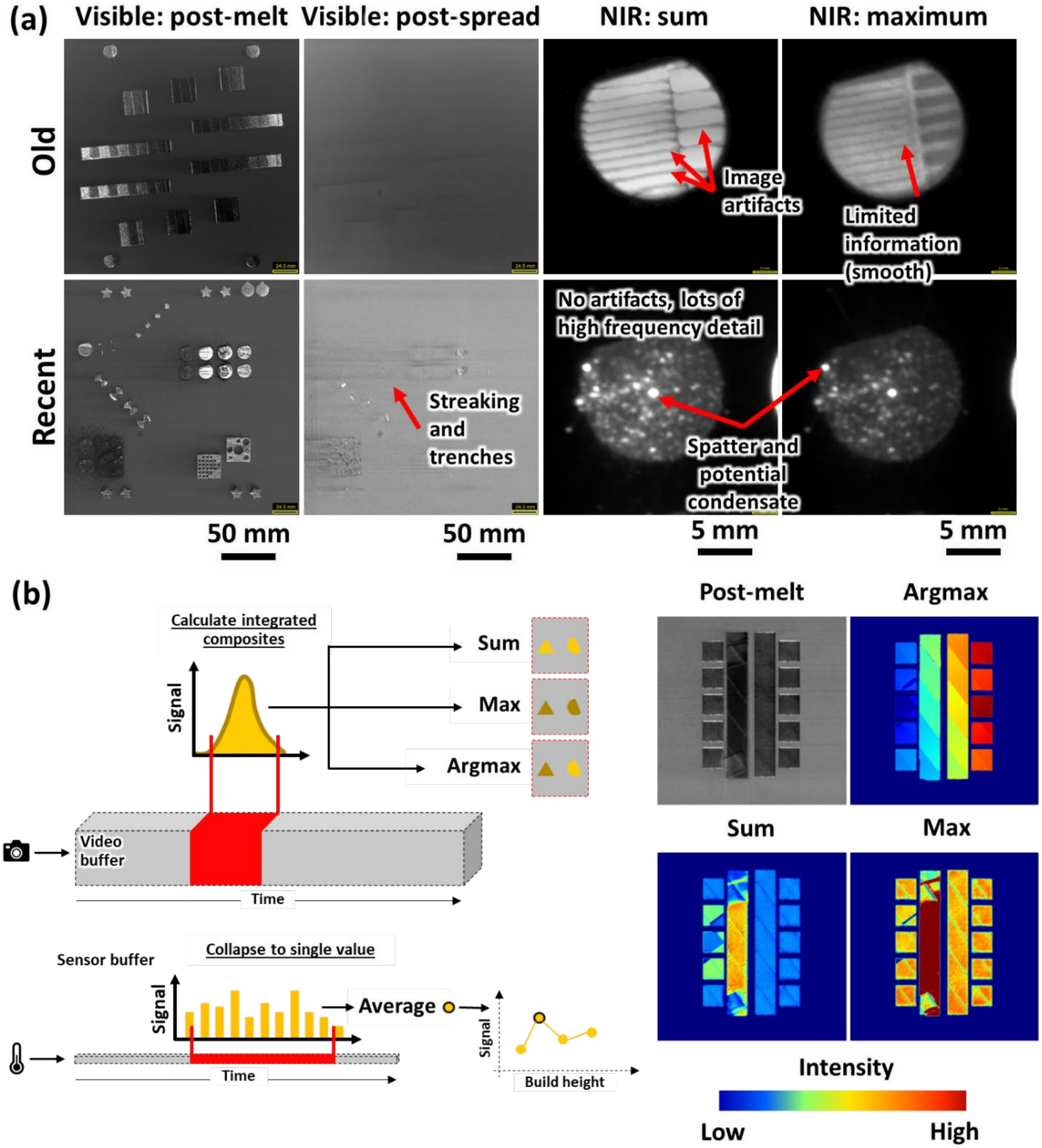

Figure 8. (a) Recent advances in camera upgrades and signal processing over the past approximately 1.5 years. Visualization of surface topology is more clear in the visible images, and artifacts in the NIR images have been mostly removed, showing more detail in recent data sets. (b) Process flow for processing the NIR image data, observing the sum and maximum intensity across the build based on a video buffer and collapsing thermal emission data into a notional thermocouple over the build height as a time series tracking.

NIR video data are processed layer-by-layer to extract thermal behavior across the build surface. Figure 8(b) shows how composite frames are calculated by performing pixel-wise operations across the image buffer to produce summed, maximum, or argmax intensity images. These composite maps provide different views of thermal response: *sum* integrates total emission, *max* identifies the hottest pixel activity during laser exposure, and *argmax* can be used to spatially track the melting order of each component during the print. The thermal intensity values can also be collapsed into a single averaged value per layer, generating a time series of build height vs. thermal emission. These views are used during postbuild analysis to identify thermal anomalies, quantify variability between parts, and classify in-layer heterogeneities that may correlate with formed flaws. The example build shown in Figure 8(b) indicates quite a bit of variability in intensity between all three composite images, which can be used to distinguish between different process anomalies.

The visible + NIR camera modalities contain spatially resolved information related to surface topography, powder coverage, and thermal emission. To extract additional insights from these data, ORNL developed the dynamic multilabel segmentation CNN (DMSCNN)—a machine learning model specifically trained to detect process anomalies from layer-wise image data collected during LPBF processing. The DMSCNN architecture is based on a type of machine learning model designed to process image data by applying convolutional filters that detect spatial patterns, such as edges, textures, and shapes, in different spatial regions of the image. These filters are trained to recognize features of interest using a large number of labeled datasets. The DMSCNN uses this architecture to process visible + NIR images as multichannel inputs, learning how specific process anomalies appear across different wavelengths. For example, surface swelling is often more easily resolved in the visible spectrum, but overheating or spatter is more prominent in NIR. Figure 9 shows a representative output from the DMSCNN, in which each pixel is classified into one of several categories, including printed material, superelevation, disturbance, and overheating. These classified regions are stored layer-by-layer and can be reconstructed into the full 3D build volume.

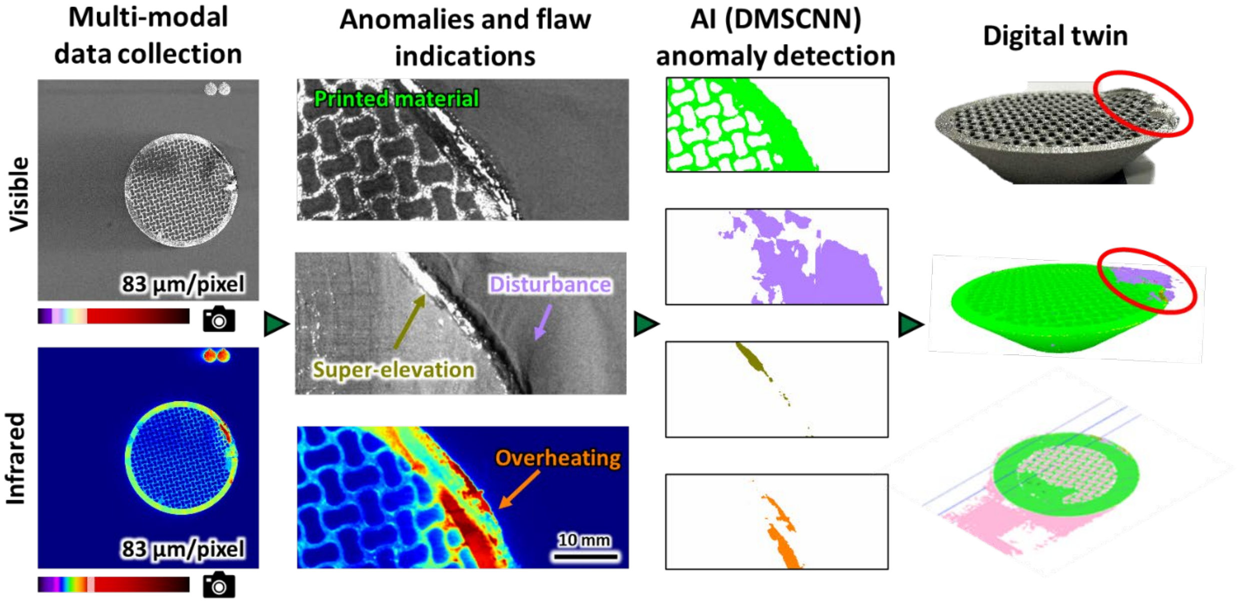

Figure 9. Processing data collection from visible + NIR camera footage using the DMSCNN to detect process anomalies and potential flaws in a printed component.

Because each segmented region corresponds to a spatial location in the component geometry, the results can be registered back to the CAD model and projected into voxel space. This ability allows localized anomalies to be traced to specific component regions and, when needed, correlated with deviations observed in the completed version of the component. As shown on the right side of Figure 9, anomalies detected by the DMSCNN, such as the identified overheating and surface disturbance on this particular component, correspond to geometry distortions in the printed component. These outputs form the front end of the Peregrine analysis pipeline.

Figure 10 highlights the broader architecture and utility of the Peregrine platform, developed at ORNL to support in situ process monitoring, data management, and machine learning–based quality control for LPBF. The platform is designed to collect, synchronize, and process multimodal sensor data during each layer of the build. Peregrine collects time-stamped data from visible + NIR cameras, machine vitals (e.g., pressure, oxygen content, temperature), and other sensors that may be deployed, such as photodiodes or pyrometers, and organizes these into a layer-wise archive. The software includes a suite of preprocessing tools to correct for perspective distortion, nonuniform lighting, and registration offsets between sensor views. Once corrected, the data are spatially aligned with laser scan path data and CAD geometry, allowing for voxel-level resolution both in the plane (*XY*) and in the build direction (*Z*). All sensor and processing metadata are stored within the component's digital thread, preserving traceability and enabling full life cycle quality tracking.

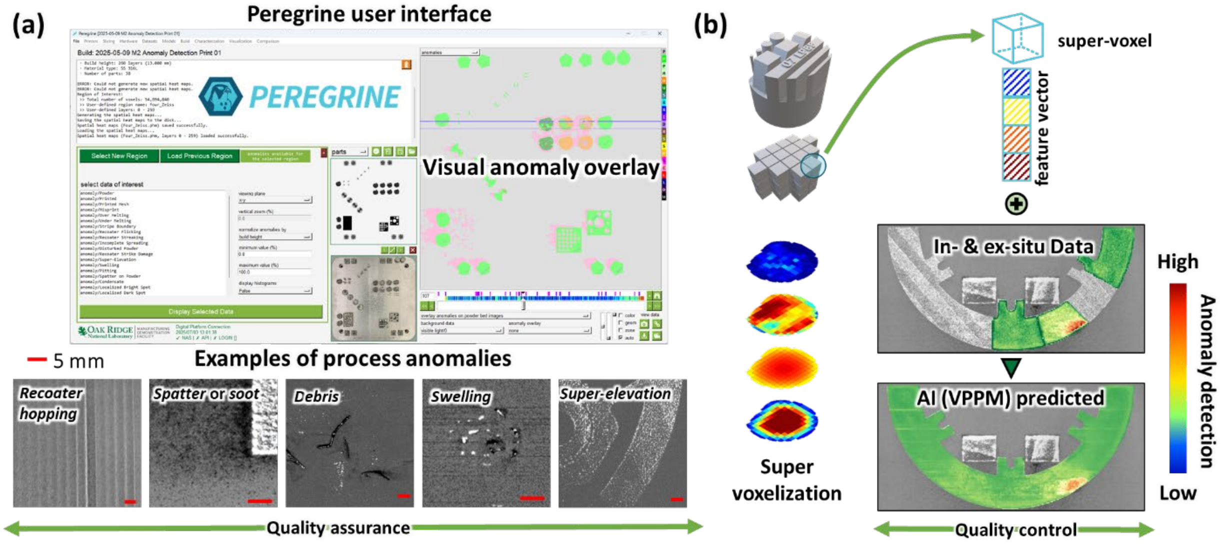

Figure 10. (a) The Peregrine UI for detecting process anomalies during in situ process monitoring of powder bed AM processes. (b) Transformation of supervoxels to compare in situ data with ex situ XCT data toward prediction of flaws during LPBF processing.

Figure 10(a) shows the Peregrine UI, which enables interactive visualization of process anomalies at the component level in real time and for the operators to use during postbuild analysis. Anomaly classifications produced by the DMSCNN can be overlaid on the component profiles, with options to filter by layer, anomaly type, or component subregion. This ability allows users to trace when and where specific anomalies occurred during the build. Peregrine currently supports classification of anomalies, such as recoater hopping, spatter/soot deposition, debris, swelling, and superelevation, among others (more detail is provided in the following section). Peregrine also collects metadata such as the processing parameters applied to each component, part template, sliced templates and scan paths, project specifics, and more—all of which goes into the digital thread for later reference to a digital twin of the component.

Beyond anomaly detection, Peregrine enables transformation of classified pixels into supervoxels, which are the core data structure for part-level analysis and quality prediction. Each supervoxel is defined as a discrete, 3D spatial region within the part, typically grouped by part ID and process subregion. Supervoxels can be around 2 to 4 group voxels, and can be scaled int size depending on the process. It combines image-derived features (e.g., anomaly type, pixel frequency), thermal emission (e.g., average emission, maximum intensity), and toolpath metadata (e.g., melt order, laser speed). These supervoxels are then used as inputs to the voxelized property prediction model (VPPM), which is a machine learning framework developed to predict localized flaws or mechanical performance loss. Figure 10(b) shows an example of the VPPM outputs mapped back onto the component geometry, identifying potential porosity hot spots that require attention. By connecting in situ observations with ex situ data such as XCT or mechanical testing, VPPM can provide predictive quality control and support flaw triage without requiring full destructive evaluation of every part.

3.2 EFFECT OF ENERGY DENSITY ON ANOMALY CLASSIFICATION

The laser energy density, as discussed in terms of VED in Eq. (1), has a profound effect on the resulting microstructure and mechanical performance of the material across the processing window in which full density can be achieved. An in-depth process optimization study was performed for LPBF of SS316 with a low-carbon (SS316L) and a high-carbon (SS316H) variant; results were detailed in other works by Massey and Nandwana et al. [23-25]. Based on the optimization study conducted for a Renishaw AM400 at ORNL, the optimized VED for SS316L and SS316H were 61.2 and 76.2 J/mm^3, respectively, as compared with the Renishaw recommended parameter for SS316L of 54.5 J/mm^3. The optimized conditions for SS316L and SS316H were based on void space measurements from XCT and downselected based on what was most stable for processing different types of geometries (e.g., bulk, overhangs, thin walls) with 99.9% theoretical density. Follow-on characterization included performing tensile testing and microscopy to confirm that these were the optimized conditions.

As a follow-on characterization to the process optimization study on SS316, large plates were manufactured for neutron diffraction at the High Flux Isotope Reactor at ORNL. The HIDRA beamline at the High Flux Isotope Reactor is designed to measure strain in metals based on the collected diffraction spectrum. Geometric specifications of the large plates that were manufactured are shown in Figure 11(a). The plates were manufactured on a Renishaw AM400 from SS316L and SS316H, as shown in Figure 11(b). Each plate had eight discrete sections that were 75 mm in length and 25 mm wide with a 5 mm gap in between each section and a 5 mm joint at the tops and bottom to maintain a *complete* part. The idea of the complete part was to demonstrate an extreme case in how stress evolution would change in a component if it experienced changes in thermal history. Each section was printed with a different VED, as reported in Figure 11(a), including the Renishaw recommended parameter and those optimized for SS316L and SS316H. The sections were printed with successively increasing VED. There were two plates printed: build direction parallel to the 12 mm thickness and to the 85 mm length. The plate printed with the build direction along the 85 mm length was used in the neutron diffraction examination.

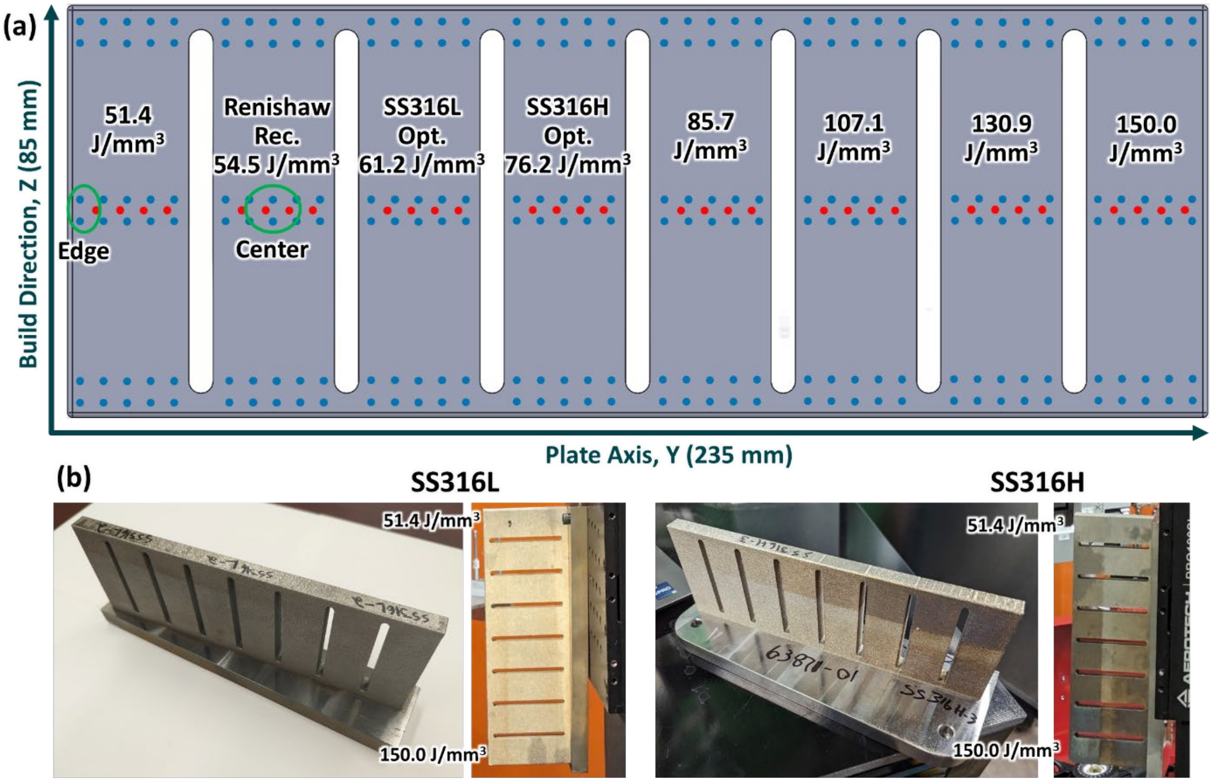

Figure 11. Large plate geometry printed from SS316L and SS316H. (a) The VED values used to print each of the eight sections, the corresponding position of each section along the plate axis, and the voxels that were collected during neutron diffraction. Plane strain was collected along the build direction. (b) The completed SS316L and SS316H plate builds, with distinct discoloration of the plate surface as VED increases.

In situ monitoring of the plates was performed during LPBF fabrication of the plates. Although the SS316H showed more discoloration on the surface of the plates compared with SS316L (Figure 11[b]), the process monitoring showed similar results. Figure 12 includes mappings from layer 49, which is approximately halfway between printing the plate that was printed with the 12 mm thickness parallel to the build direction. An unexpected process anomaly was observed here, as indicated by the red box in Figure 12. The plate was printed with increasing VED reading from left to right in the images. The most critical process anomaly overlays are given, but a complete overlay of all anomalies is shown in Figure 12(b). One thing to note is that dropped NIR pixels occurred at the low-VED end of the plate, in which the DMSCNN could not process into any anomaly classification.

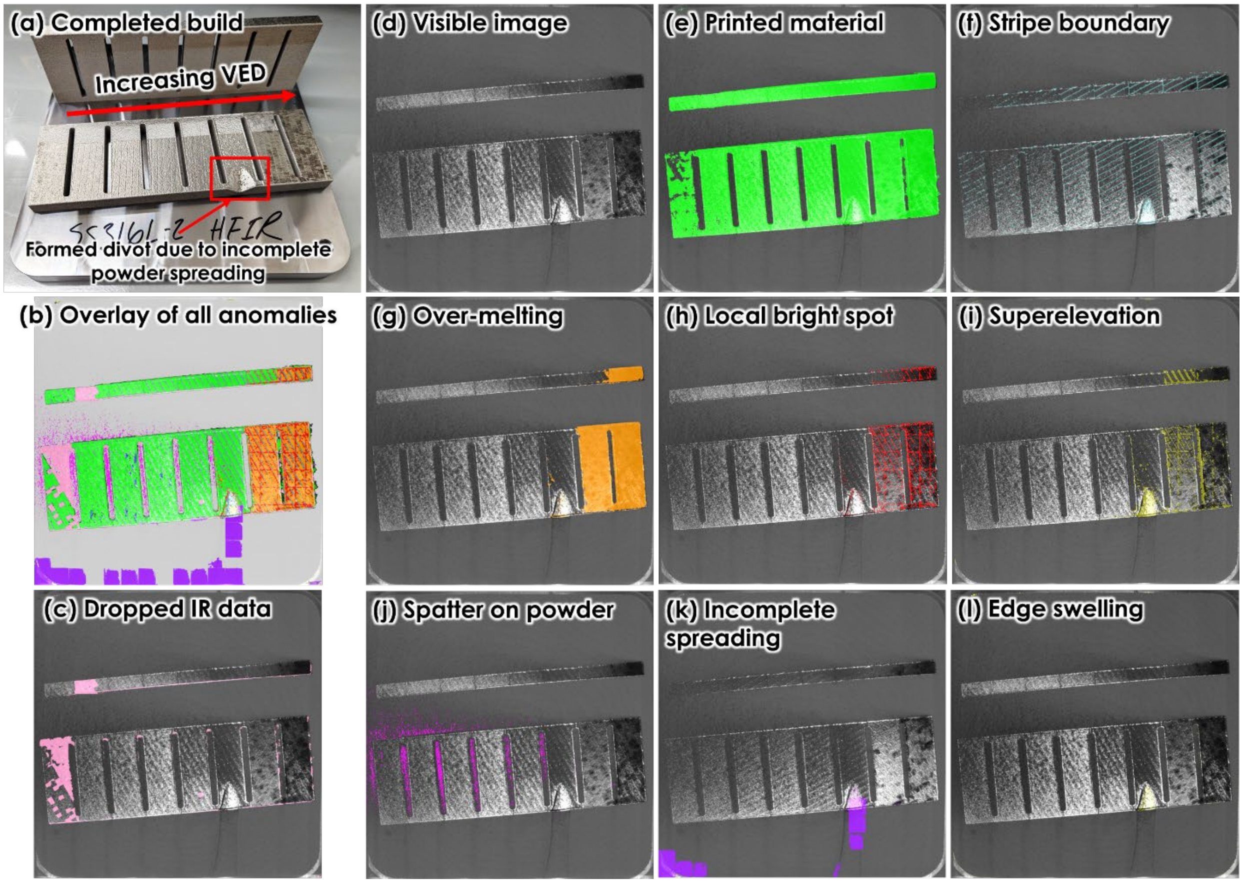

Figure 12. Locating process anomalies and other features on the postmelt visible image taken at layer 49 for the build shown in (a). (a) The completed build consisted of two identical plates—plate axis printed perpendicular and parallel to the build direction—with eight discrete sections, each fabricated with a different energy density, as described in Figure 11. The mappings shown are as follows: overlays of (b) all anomalies, (c) dropped infrared data that could not be classified with the DMSCNN, (d) the unadulterated visible image, (e) printed material, (f) stripe boundaries (5 mm widths), (g) overmelting, (h) localized bright spots in NIR, (i) superelevation, (j) powder spatter, (k) incomplete spreading, and (l) edge swelling.

Figure 12(e) shows that the majority of regions in which printed material was located for the two plates in the build could be identified by the DMSCNN, and the striped patterns shown in all the images are artifacts from the stripe boundaries identified in Figure 12(f). Overmelting was observed on the right two sections shown in Figure 12(g), which happens to correspond to the high VED used on those two sections. As a consequence, a number of localized bright spots were observed in these regions, similar to potential hot spots mentioned in Figure 5. The excessive overmelting caused superelevation to be idenfied across the two sections, as shown in Figure 12(i). Although, the DMSCNN did not know whether the entire field should be considered superelevation. However, it clearly knew that the overmelting was causing distortion in the two sections. The excessive melting on the rightmost side of the build showed a high density of powder spatter particles in Figure 12(j), which likely influenced the macro- and microstructure of the low-VED sections.

As indicated in Figure 12(a), a critically serious process anomaly occurred; a divot formed on the third section from the right, becoming nonconforming to expected geometric dimensions. The divot appeared to be caused by powder starvation in that area, as indicated by incomplete spreading in Figure 12(k). Although some uneven detection of incomplete powder spreading occurred in layer 49, Figure 12(k) does show that the divot was identified to be the result of incomplete powder spreading. Edge swelling resulted from the divot formation, as shown in Figure 12(l), because the height of the divot was significantly different than that of the surrounding build. The DMSCNN did not appear to recognize a negative change in height and did identify the divot as superelevation [Figure 12(i)] but nonetheless indicated that that the divot was real.

Figure 13 shows the calculated residual strain (ε) for SS316L and SS316H plates based on the change in atomic spacing measured by neutron diffraction spectrums. These plates were originally fabricated to correlate processing parameter VED windows for SS316, but also serve as a benchmark for linking in situ process anomalies to build-scale thermal stress outcomes. Figure 13(a) and Figure 13(b) give the residual strain in the build direction, mapped across the build height for each VED; the zero value of the strain is set at the color orange, with blue corresponding to more compressive stress and red indicating higher tensile stress. Increasing the VED for both SS316L and SS316H results in deeper and more intense compressive strain zones at the center of each section, with sharp tensile strains appearing on the edges of section. Moreover, the bottom of each section is consistently closer to a neutral strain as compared to the middle or top along the build height. There may appear to be progressively more tensile strain in the SS316H over that of the SS316L, but it is difficult to distinguish in the maps.

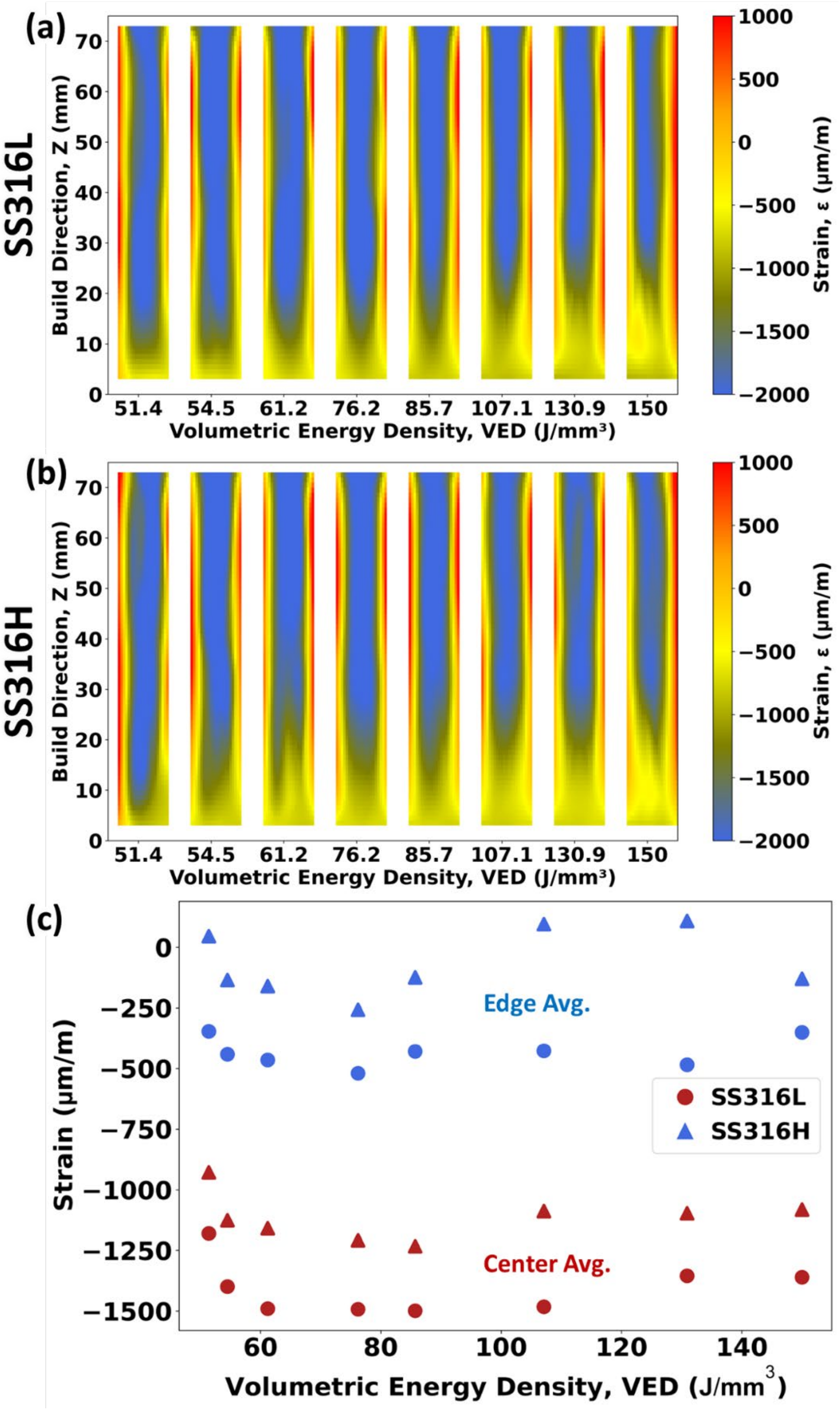

Figure 13. Residual strain mapped using neutron diffraction for the (a) SS316L and (b) SS316H plates shown in Figure 11. (c) Averaged stain across the center of the plate [indicated by the red dots in Figure 11(a)] for the SS316L and SS316H at the (blue) edge and (red) center of each section.

Figure 13(c) quantifies the strain values at the center and edges of each section, extracted from the regions of interest marked by the green circles in Figure 11(a): the edge corresponds to average of the outermost voxels, and the center was the average of the rest of the voxels away from the edge. Across all energy densities, SS316H shows higher compressive strain, particularly at the center of the plate—a region prone to thermal accumulation and geometric distortion. This result is consistent with earlier observations from Peregrine in Figure 12, which showed that swelling and overmelting anomalies were more common in SS316H, particularly under high-VED conditions.

These data provide a critical link between what is observed in situ during printing and the mechanical state of the material postbuild. Process anomalies such as swelling, superelevation, and laser overheating as mapped in real time via visible + NIR imaging now have a confirmed spatial correlation with postbuild strain. These relationships validate the use of Peregrine anomaly maps as predictive indicators of downstream material behavior and support the broader qualification strategy laid out in the AMMT program.

Furthermore, this work highlights the importance of real-time sensing in identifying limiting processing regimes. Although neutron diffraction provides a high-fidelity strain measurement, it is time- and resource-intensive. In contrast, in situ monitoring tools such as Peregrine and fringe projection offer a scalable method to detect the onset of these strain-driving features during the build itself. With sufficient anomaly classification resolution and sensor coverage, in situ tools could eventually replace or prescreen for more intensive ex situ validation methods. Ultimately, this correlation between energy input, anomaly formation, and strain development helps close the loop on the AMMT qualification pathway: sensing informs modeling, modeling identifies risk, and risk informs build strategy. The identification of high-VED + geometry combinations as a clear process risk demonstrates progress toward the milestone's goal of establishing a defect-aware, data-driven manufacturing approach for nuclear-grade materials.

3.3 CALIBRATION BUILDS

Many process anomalies can be identified and classified for LPBF and are well-summarized elsewhere [31, 52]. Some common examples to identify are shown in Figure 10(a): recoater hopping occurs when the recoater blade impacts a sharp feature and lifts momentarily, and repeated interaction can evolve into recoater streaking, which causes trenches or uneven powder layers. Spatter results from material ejection during melting and its redeposition, or it can vaporize and condense back to a solid (referred to as *condensate*) can affect subsequent layers. *Debris* refers to loose particles or fragments detached from the part. Superelevation and swelling both indicate material extending above the expected build plane and can result in recoater interference or uncontrolled energy absorption.

Training the DMSCNN for a specific LPBF system typically requires multiple builds to achieve stable and reliable classification performance. To accelerate this process, calibration builds were designed with asymmetric geometries and overhang-heavy features that are known to trigger process anomalies. Figure 14 shows calibration builds performed on the Renishaw AM400 and M2 Concept Laser, each featuring stepped transitions, curved voids, sharp corners, thin-walled structures, and unsupported spans. Many geometries intentionally violate good design-for-AM rules to expose the model to as many edge cases as possible, including overhangs printed directly onto powder with little or no thermal conduction path.

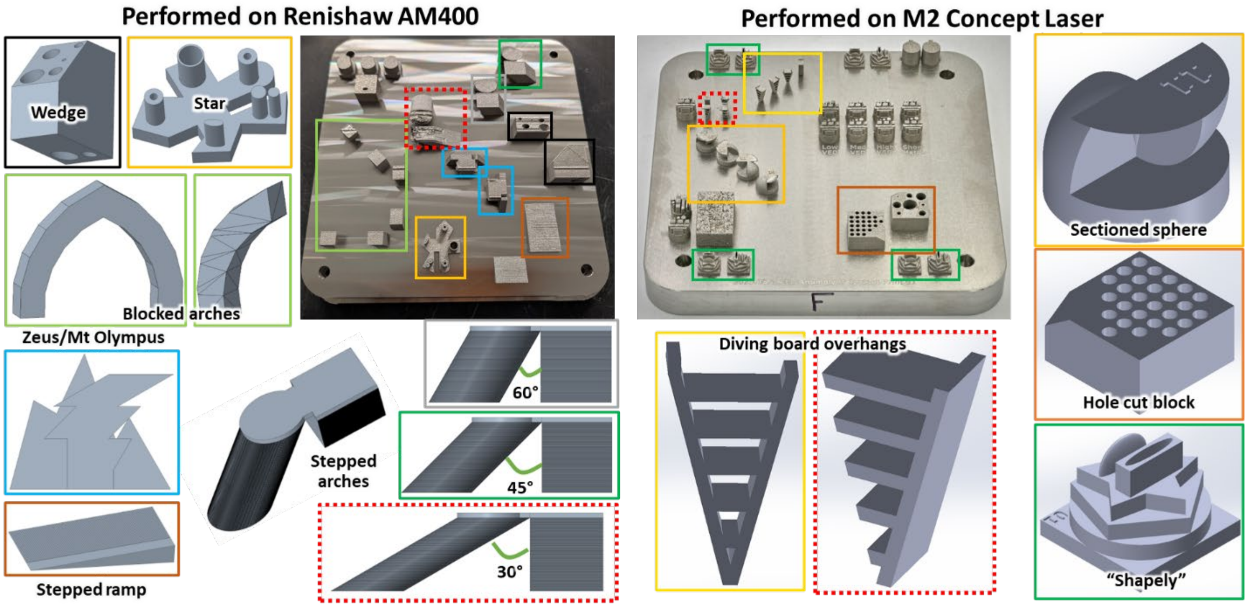

Figure 14. The different geometries used in the calibration builds to induce different types of process anomalies across different LPBF systems to rapidly train the DMSCNN for each machine.

Figure 15 shows selected layers from these builds, highlighting how the DMSCNN identifies and tracks anomalies through the build height. The most limiting geometry and processing condition for the two builds is detailed in Table 1. On the M2, where the DMSCNN was already well trained, the anomaly segmentation appears more comprehensive and consistent across layers. In contrast, the AM400 build shows fewer segmented anomalies—partly due to its newer model—and ultimately failed to complete because of build instability.

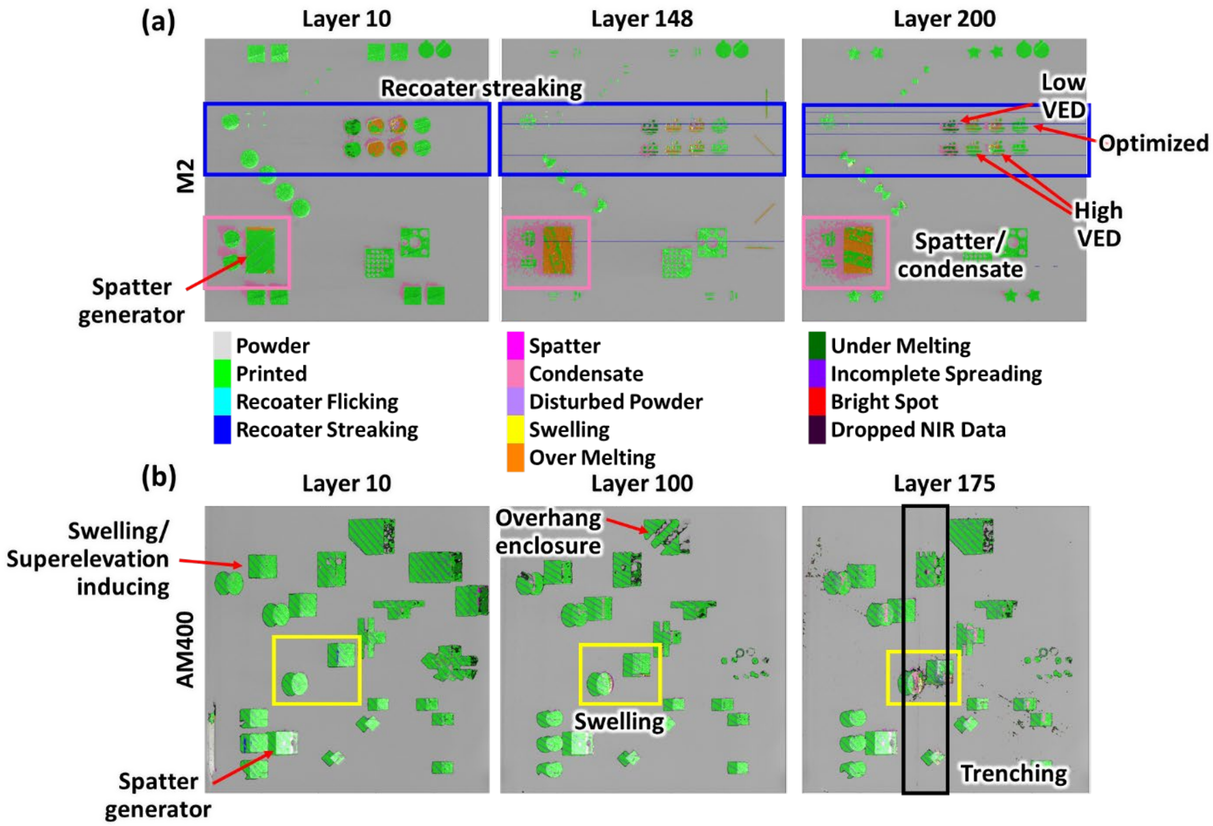

Figure 15. Overlaid anomalies on printed material for selected layers at the beginning, middle, and toward the end of a print for two builds on the (a) M2 and (b) AM400. Particular process anomalies are observed and followed throughout the build that could be used to indicate where flaws might occur.

Table 1. Most limiting geometry and processing condition for the two calibration builds presented in this report

Geometry	Machine	Process parameter	Detected anomalies	Outcome
Diving board	M2	High VED	Recoater streaking, swelling	Thermal interference with adjacent parts
Stepped arch	AM400	Standard VED	Swelling, debris	Build failure

Several key geometries were added specifically to test the repeatability and progression of anomalies. On the M2, the sectioned sphere and diving board geometries were both designed to induce swelling. The sphere offers a continuous heat conduction path; the diving boards are cantilevered and isolated, sitting entirely on powder. As shown in Figure 15(a), the diving boards triggered significant recoater streaking (shown in the blue box), which led to thermal accumulation and swelling in nearby parts. In the same build, two clusters of Zeiss geometries were used to study the effects of VED and spatter accumulation. One region included high/low–energy density variants and showed exaggerated swelling on high-VED components when located near streaking. A second Zeiss pair was positioned near a spatter generator, which had a thick layer profile designed to eject powder. Over time, condensate buildup was visibly higher in this area, confirming that recoater-driven transport can spatially bias powder bed contamination.

At the time of this build, the AM400 DMSCNN had undergone minimal supervised training, resulting in underdetection of process anomalies that were later confirmed through postbuild inspection. The stepped and blocked arches tested whether support angles and thermal bridging would lead to deformation. The stepped arch at 30° became unstable early in the build. Swelling was first detected along the edges, as tracked by the yellow box in Figure 15(b); as the arches met at the top layer, the geometry collapsed, leading to debris formation and powder trenching. Other geometries, such as the Zeus/Mt. Olympus feature, tested sharp edges and multiple angles for recoater hopping, and the stepped ramp and star geometries tested resolution and debris shedding. The wedge was designed to trap heat in enclosed voids, simulating internal overhangs, and was monitored for swelling or distortion over time.

The combination of unsupported overhangs and high VED in the M2 build produced repeatable recoater streaking and swelling. In particular, the diving board and arch geometries revealed how insufficient conduction paths combined with energy accumulation can create high–defect risk conditions. These calibration builds serve not only to train the DMSCNN for a given machine but also to understand how localized anomalies develop across the build volume. When paired with part geometry and location, the anomaly maps provide a way to trace conditions that may cause subsurface defects or influence mechanical performance. The data collected in this work supports future VPPM training and helps identify when targeted postbuild inspection may be required.

4. EVALUATION OF PHASE3D FRINGE PROJECTION

4.1 FRINGE PROJECTION FOR IN SITU MONITORING

Fringe projection is an optical technique that uses structured light to reconstruct the surface topography of an object. The approach is similar to confocal profilometry but operates at standoff distances compatible with LPBF systems and does not interfere with the build process. Unlike visible imaging or thermal sensors, fringe projection provides a direct measurement of surface height, even when reflectivity or texture varies. Several groups [45-49] have demonstrated the capability of fringe projection for layer-wise anomaly tracking, surface flatness evaluation, and postmelt topography analysis. For instance, Zhang et al. [48, 49] showed that a well-calibrated projection and phase extraction system could identify subtle powder recoating issues, overmelting-induced protrusions, and spatter deposition zones based on localized surface height spikes.

In fringe projection, a pattern of alternating light and dark bands (i.e., fringes) is projected onto the powder bed or build surface and captured using a camera at a known angle. Figure 16(a) shows examples of projected fringe patterns for a smooth surface compared with a simulated powder bed surface as well as that of the laser-melted layers; these are simulated curves drawn in Python v3.13. Deviations from a flat and smooth surface cause the fringes to become distorted. These distortions are converted into height measurements using phase shifting and phase unwrapping algorithms. Figure 16(b) shows an example of a fitted phase projection curve for the flat and smooth surface [shown in Figure 16(a)] as it compares with the projection; both curves fall on top of each other. Figure 16(c) shows the case of a fitted curve taken from the projection over the rough surface of the powder bed [shown in Figure 16(a)], which is noisy and has many local maxima and minima compared with the smooth curve of the original projection. The resulting phase map corresponds to relative surface height across the field of view and provides a noncontact, layer-resolved method for detecting surface roughness, geometry deviation, or melt-induced distortion.

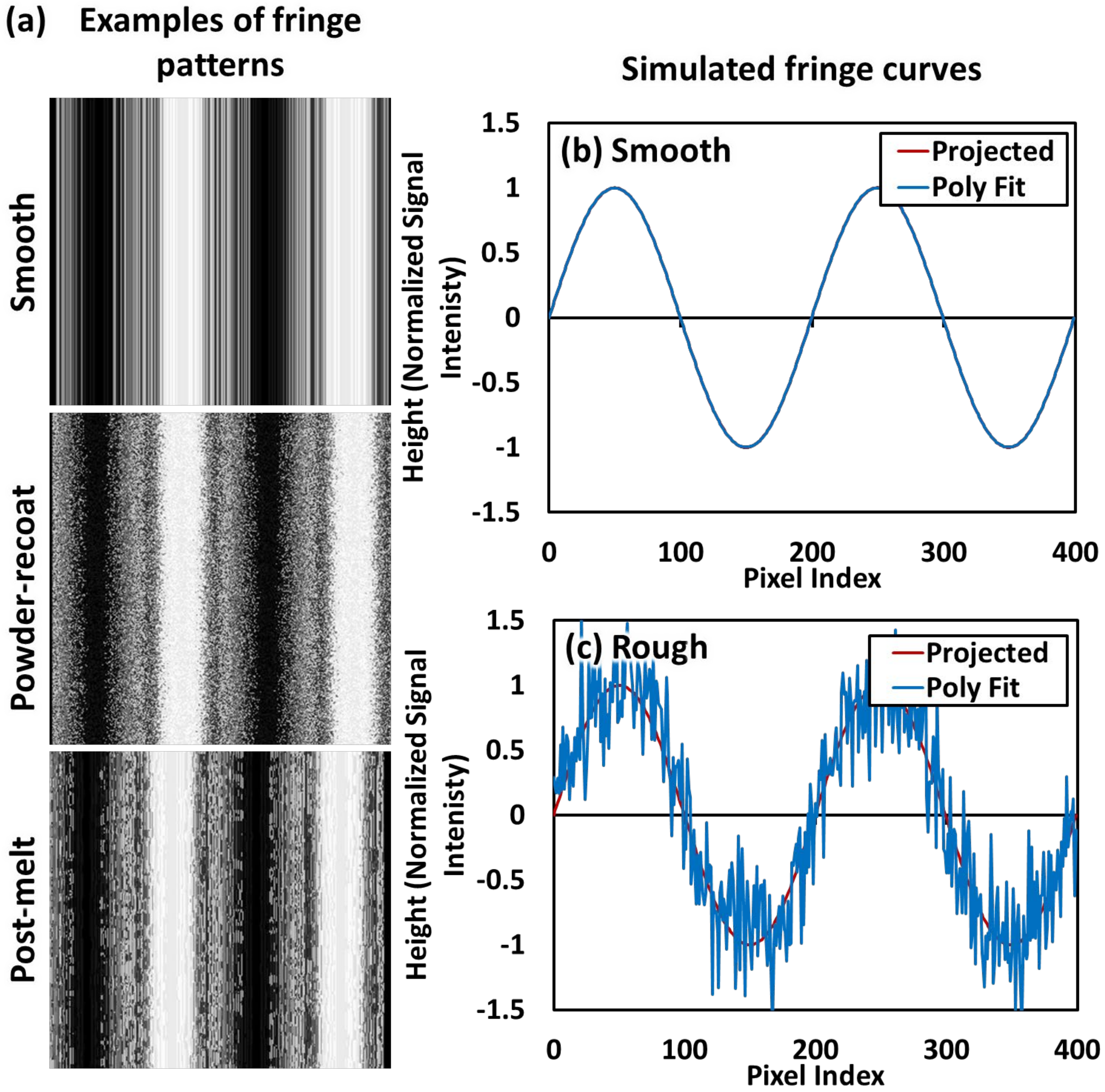

Figure 16. Examples of (a) projected fringe patterns and (b) resulting sinusoidal curves on different surfaces. The generated profiles are simulations generated in Python v3.13.

To quantify the distortion, the observed fringe signal intensity $I(x)$ is compared with an ideal fitted profile. A common starting point is a linear fit across small fringe windows:

$$I(x)_{\text{fit}} = a_0 + a_1 x, \tag{3}$$

where a_0 and a_1 are fit parameters that approximate a local baseline based on the average value of intensity for a pixel x. However, to capture curvature and distortion with higher fidelity, a polynomial fit of order n is typically used:

$$I(x)_{\text{fit}} = a_0 + a_1 x + a_2 x^2 + a_n x^n = \sum_{i=0}^{n} a_i x^i. \tag{4}$$

Polynomials to the third or fifth order are most commonly used to model the expected fringe curvature under ideal conditions on a smooth surface. A fifth-order polynomial was used for the data in Figure 16(b) and Figure 16(c). The residual between the observed signal and the fit is then used to estimate surface roughness or local deformation using a linear approximation or a more accurate sum of least squares fit:

$$\epsilon(x) = I(x) - I(x)_{\text{fit}}. \tag{5}$$

$$\epsilon(x) = \sum\nolimits_{x} (I(x) - I(x)_{\text{fit}})^2 \tag{6}$$

These residuals can be mapped layer-by-layer and used to construct a height deviation map across the build surface. When combined across multiple rows or columns, these deviations can be mapped layer-by-layer and converted with a proper calibration to physical height differences with accuracy of approximately 1–10 µm. The surface topology of every layer could potentially be stacked into a 3D reconstruction of the component being printed. Process anomalies and flaws can be identified based on this 3D reconstruction.

4.2 DEPLOYMENT OF FRINGE PROJECTION ON RENISHAW AM250

LPBF printer OEMs typically provide some form of monitoring (e.g., photodiodes, cameras), but these are not yet reliable enough to serve as quality assurance–grade tools. Few commercial solutions exist for true in situ monitoring of powder bed processes. One such technology is being developed by Phase3D (also known as Additive Monitoring), a Chicago-based start-up spun out of Argonne National Laboratory. Phase3D holds a patent [53] on a fringe projection–based sensor suite capable of generating micrometer-scale 3D surface reconstructions using structured light [54]. Phase3D's sensor suite technology has been deployed in projects with the US Air Force, NASA, and other academic partners. This fringe projection–based sensor suite complements the currently deployable visible + NIR imaging by adding a full-surface height mapping capability. Critically, reconstructed surfaces could be compared directly with XCT scans to investigate in situ detectability of voids and lack-of-fusion flaws. Therefore, the Fringe Projection system was chosen for investigation under the AMMT program.

A Renishaw AM250 unit was chosen for installation of the Fringe Projection sensor suite, which includes a green polarized light projector, a visible camera to capture images of the projection, and a photodiode for triggering purposes. Figure 17 shows the projector and camera combo being mock-up mounted on the top of the AM250's build chamber; note that the sensor suite is not inside the build chamber but rather on top looking downward through a sight-glass. The projector and visible camera have been situated to overlay and capture the entire 250 × 250 mm build plate. The installation of the sensors was completed as of March 2025, but issues with triggering and calibrating the system delayed full use of the system until June 2025. Two calibration builds were completed, using similar geometries as that shown in Figure 14, to induce process anomalies.

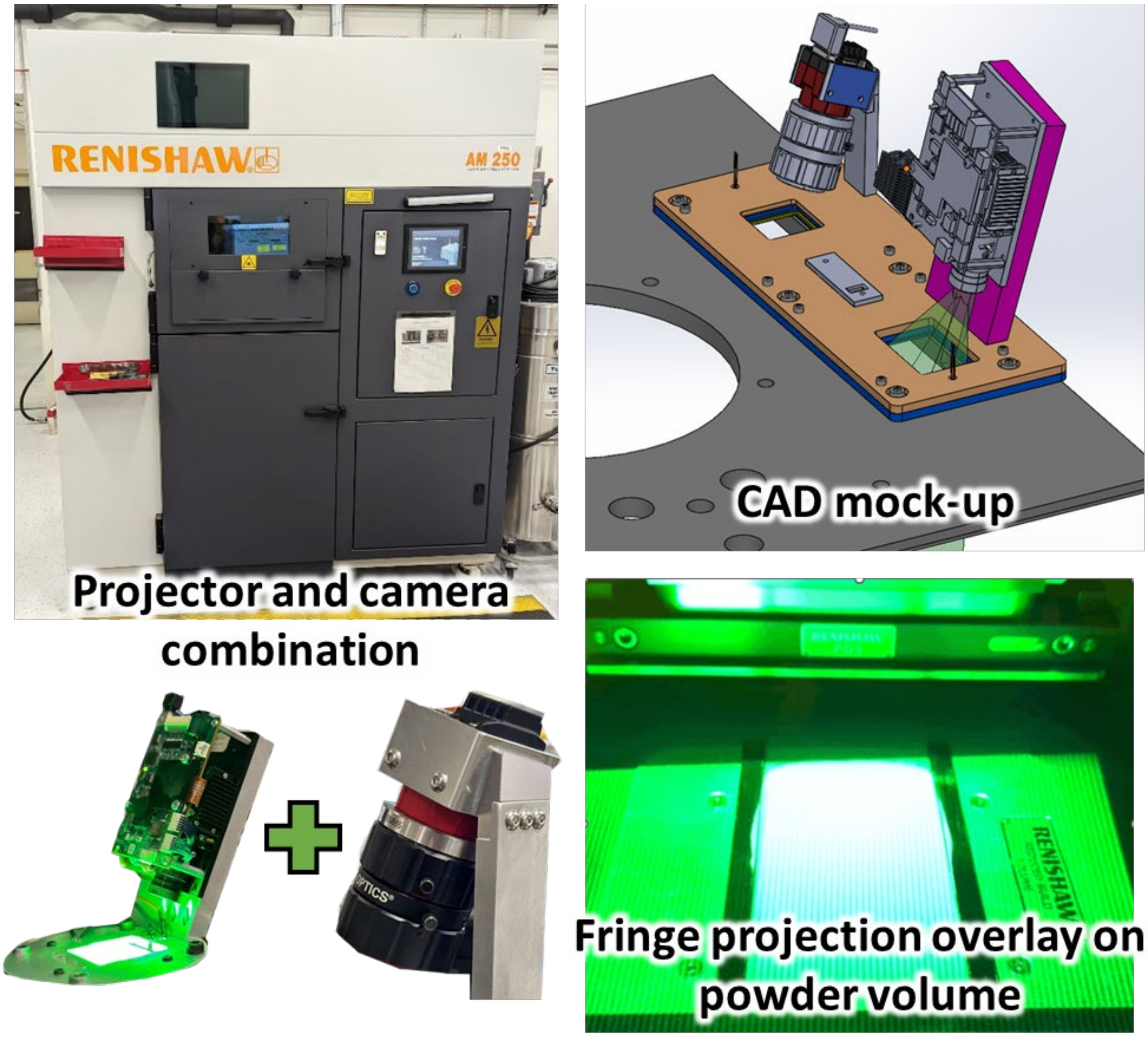

Figure 17. Deployment of the Phase3D fringe projector + visible camera setup on a Renishaw AM250.

The Fringe Projection system is controlled via the Fringe Operator software, which provides real-time and postbuild inspection tools. Although the details of Phase3D's proprietary data acquisition and phase processing pipeline are not disclosed, the resulting dataset includes visible camera images captured after powder recoating and after laser melting, as well as a structure file containing fitted phase residuals and surface height maps. Figure 18 illustrates the Fringe Operator interface, which includes (1) a surface roughness height map (right), which can be stepped through layer-by-layer; (2) a 3D reconstruction of the part using the topographical height data (center); and (3) a anomaly detection panel (left), which currently flags five anomalies by type, depth, and location. At the time of writing, detected anomaly types include streaks and hops. Although automated detection is currently limited, additional labeled examples could be used to expand detection capabilities by training a CNN to classify anomalous surface morphologies across layers.

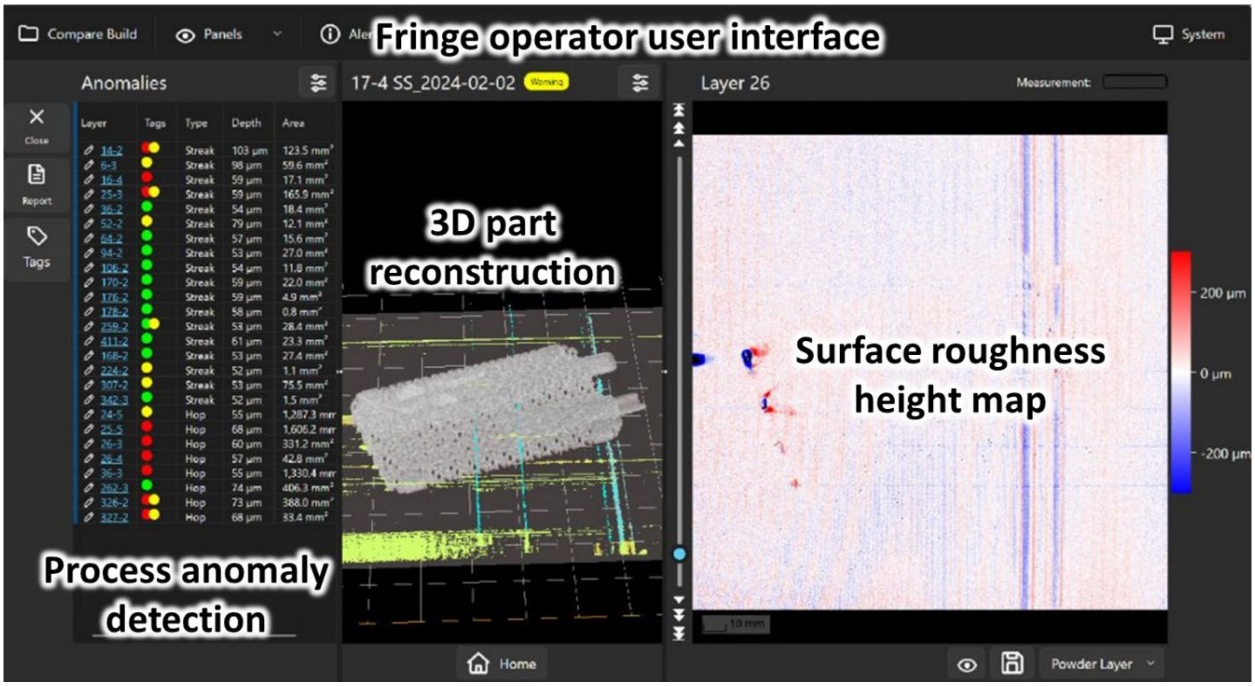

Layer	Tags	Type	Depth	Area
14-2	🔴🟡	Streak	103 µm	123.5 mm²
6-3	🟡	Streak	98 µm	59.6 mm²
16-4	🔴	Streak	59 µm	17.1 mm²
25-3	🔴🟡	Streak	59 µm	165.9 mm²
36-2	🟢	Streak	54 µm	18.4 mm²
52-2	🟡	Streak	79 µm	12.1 mm²
64-2	🟢	Streak	57 µm	15.6 mm²
94-2	🟢	Streak	53 µm	27.0 mm²
106-2	🟢	Streak	54 µm	11.8 mm²
170-2	🟢	Streak	59 µm	22.0 mm²
176-2	🟢	Streak	59 µm	4.9 mm²
178-2	🟢	Streak	58 µm	0.8 mm²
259-2	🟢🟡	Streak	53 µm	28.4 mm²
411-2	🟢	Streak	61 µm	23.3 mm²
168-2	🟢	Streak	53 µm	27.4 mm²
224-2	🟡	Streak	52 µm	1.1 mm²
307-2	🟡	Streak	53 µm	75.5 mm²
342-3	🟢	Streak	52 µm	1.5 mm²
24-5	🟡	Hop	55 µm	1,287.3 mm
25-5	🔴	Hop	68 µm	1,606.2 mm
26-3	🔴	Hop	60 µm	331.2 mm²
26-4	🔴	Hop	57 µm	42.8 mm²
36-3	🔴	Hop	55 µm	1,330.4 mm
262-3	🟢	Hop	74 µm	406.3 mm²
326-2	🔴🟡	Hop	73 µm	388.0 mm²
327-2	🔴🟡	Hop	68 µm	33.4 mm²

Figure 18. Fringe Operator UI, which allows for visualization of the surface roughness height map, a 3D reconstruction of the part geometry, and any detected process anomalies within the build [54].

Figure 19 shows a summary of a calibration build that was performed on the AM250 to evaluate the performance of the installed Fringe Projection system using a test geometry specifically designed to induce localized swelling, powder streaking, superelevation, and, eventually, warpage. The geometry was an upside-down pyramid intended to produce upward growth anomalies because of its overhanging geometry and sharp slope transitions, which can challenge powder spreading and thermal control. The build coupon was approximately 30 mm in lateral size and fabricated from an advanced SS alloy using a powder layer thickness of 30 µm. Layer height data shown in Figure 19 were for two specific layers: layer 50, in which early signs of superelevation were visible, and layer 80, in which significant surface elevation deviations had accumulated. These two layers are representative of the progressive deviation from nominal height that occurs as geometric constraints amplify layer-to-layer surface distortion.

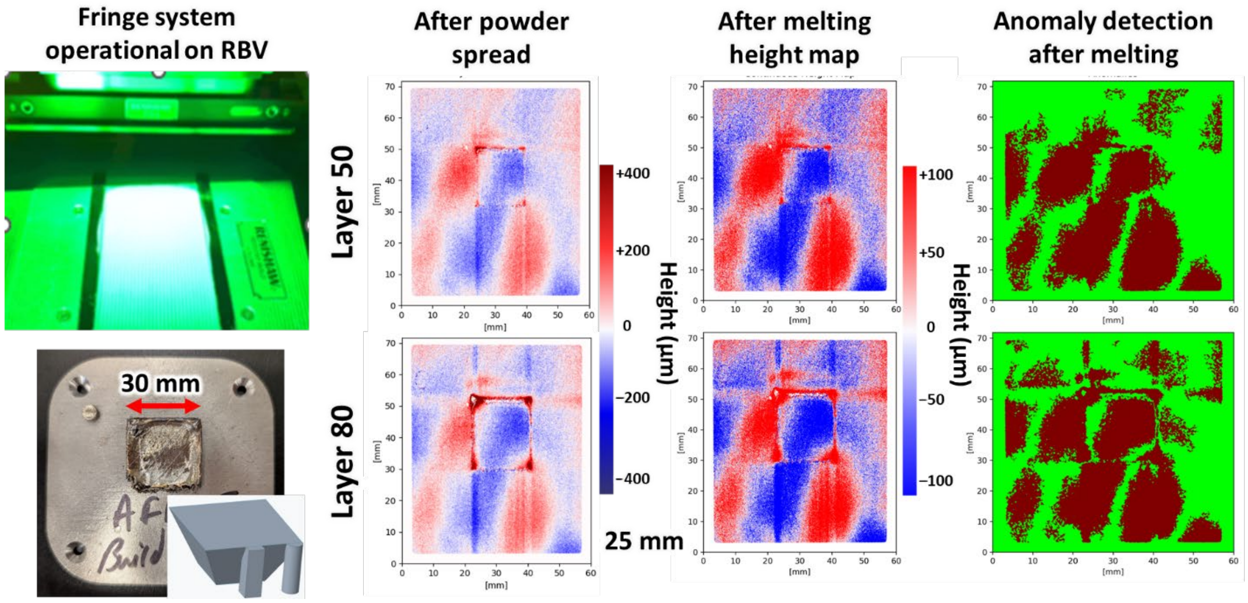

Figure 19. In situ monitoring results from the Phase3D Fringe Projection system during a calibration build on the AM250 using a geometry designed to induce superelevation via an upside-down pyramid structure. The Fringe Projection system successfully captured surface height changes after powder recoating and melting for layers 50 and 80. In both cases, significant roughness and superelevation are visible, with height deviations reported as exceeding ±400 µm by layer 80. However, the anomaly detection logic in the Fringe Operator software failed to flag these features as anomalies despite their severity. This result suggests that the current detection model may require threshold refinement to capture large-area, gradual elevation changes not categorized as traditional *streaks* or *hops*.

The first two surface height maps shown in Figure 19 were analyzed using the postrecoat and postmelt images. The red and blue coloring indicate height deviations, which were ±400 µm in the after powder spreading and ±100 µm profiles after melting. These maps would suggest a high degree of surface thickness difference along the entire powder bed. The postmelting height maps reveal similar elevation patterns as the postrecoat maps, which could imply partial flattening of surface features caused by laser melting but may just indicate artifacts from the fringe projection + visible imaging. Both maps, however, did indicate peripheral differences at the contour profile of the square that makes the pyramid.

Most critically, the rightmost column of Figure 19 presents the output of the Fringe Operator's process anomaly detection module, which attempts to segment the surface into regions flagged as anomalous (red) or normal (green) based on internal thresholds. The anomaly detection mapping was ambiguous and did not appear to show any profile of the component and no process anomalies identified. Despite the evident height changes captured in the raw data, the system may not still be fully calibrated to properly classify any regions as anomalous at layer 50 and only partially flagged minor areas by layer 80. This result underscores a key limitation of the current detection model: it is biased toward identifying discrete, sharp defects such as streaks or spatter events and underperforms when presented with gradual, continuous deformation such as superelevation. The inability to detect these progressive surface deviations highlights the need for enhanced detection algorithms or supervised learning approaches that can leverage height map history and shape context rather than relying solely on threshold-based filters.

Because of some of the limitations of the Fringe Operator software, a workspace was created with Peregrine to read in the visible images and residual data file. A second calibration build that was analyzed with the DMSCNN within Peregrine is shown Figure 20. The build was performed using a combination of overhangs and geometric offsets to induce failures using the stepped arch and Zeus/Mt. Olympus geometries described in Figure 14. The same fringe projection sensor suite was used to monitor the build, but this time, a direct comparison was made between output from Phase3D's Fringe Operator and Peregrine. Figure 20(a) shows the build layout and result after the build was stopped. Unlike the calibration build performed in Figure 14, the stepped arch was not the failure point, but the Zeus/Mt. Olympus geometry caused the build to be stopped because of excessive warpage cutting into the wiper/reacoater blade.

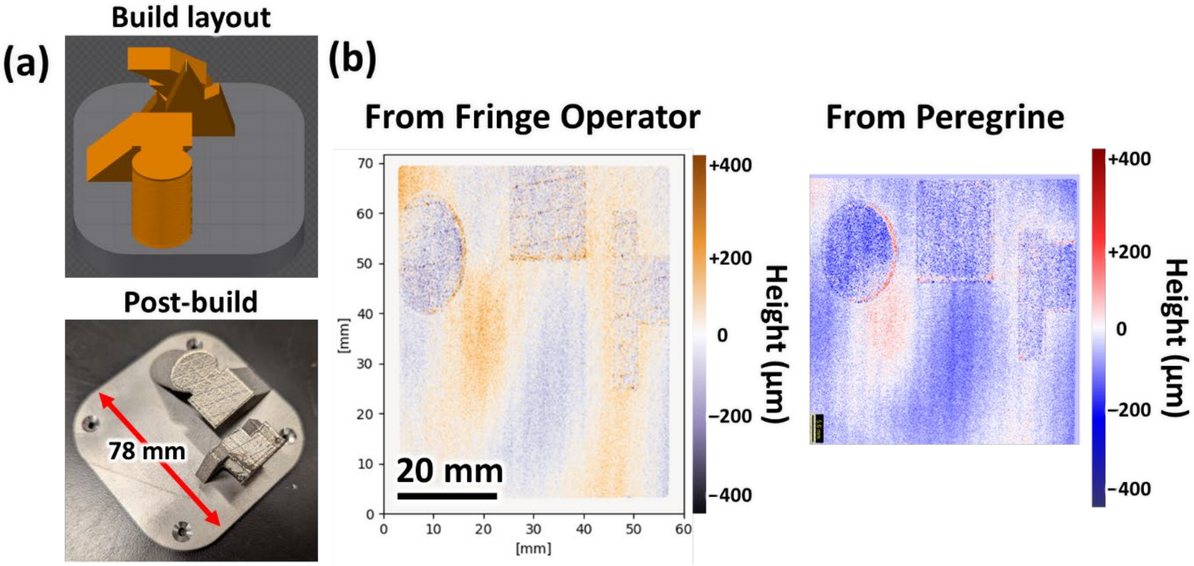

Figure 20. (a) Calibration build performed on the AM250 with the fringe projection system. (b) Comparison in reading the fringe height maps between the Fringe Operator software and Peregrine.

Figure 20(b) shows a height map comparison taken from a layer near the end of the build, visualized using Fringe Operator (left) and Peregrine (right). Peregrine performs no calculations or additional analysis on the raw data. The two maps appear qualitatively similar, with consistent height deviations observed across the central region and right-side overhang features. Considering the layer thickness is 30 µm, it is difficult to understand the large deviation in build height, which was an order of magnitude higher than the layer thickness.

Figure 21(a) shows average roughness postmelt over build height from Peregrine, with height deviation increasing gradually over time until the build failed at approximately 12.3 mm (just over halfway through the expected 20 mm build). This trend was visible in the fringe projection data as well, although the roughness visualization tools in Fringe Operator are still under refinement. Figure 21(b) shows the process anomalies detected overlaid on the part contours from layer 280 (~8.4 mm) after the peak change in surface roughness was observed at 5–6 mm. Moreover, the overheight seemed to appear around the edge of the ovular portion of the stepped arch, as shown in Figure 21(c). Even though a false positive was observed in the powder bed, as indicated by the white box in Figure 21(b) and Figure 21(c), the identification of the overheight on the ovular shape is consistent with the swelling observed in the ovular geometry of the step arch in Figure 15(b).

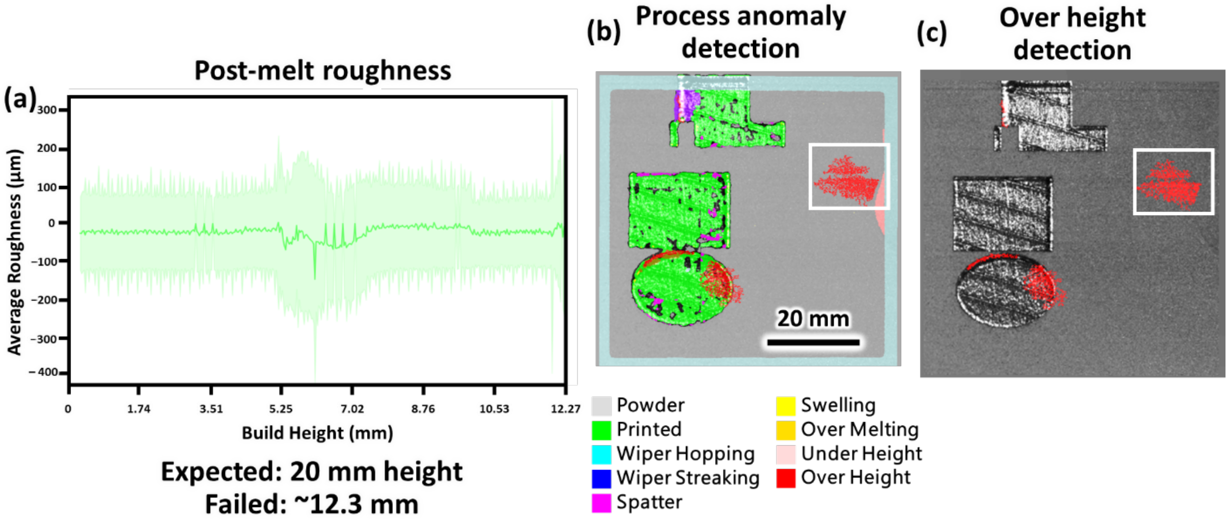

Figure 21. (a) Visualization of roughness changes throughout the build, (b) process anomalies detected using Peregrine at layer 280 (8.4 mm), and (c) identification of overheight at layer 280. The white box in (b) and (c) indicates a region of false positives in the software.

These results demonstrate that fringe projection provides high-resolution height data suitable for tracking the evolution of surface features and detecting deformation in real time. Although the current detection logic within Fringe Operator remains under development, the core hardware and reconstructed data are already capable of supporting layer-wise analysis and failure prediction. When used in combination with Peregrine or other machine learning models, fringe projection offers a powerful tool for identifying and triaging process anomalies in LPBF.

5. LONG-WAVELENGTH INFRARED CAMERA DEPLOYMENT

5.1 BACKGROUND AND MOTIVATION

Long-wavelength infrared (LWIR) thermography has been recognized as a potential tool for in situ monitoring of LPBF processes [55, 56], offering advantages in capturing thermal behavior that is often difficult or impossible to detect in visible or NIR imaging. Although visible and NIR systems are ideal for detecting high-temperature melt pool dynamics, LWIR excels at mapping broader thermal fields associated with cooling, heat accumulation, and powder bed behavior. For example, previous work has used active LWIR thermography to estimate powder layer thickness and thermal conductivity by analyzing the surface's thermal response to laser exposure and cooling. This work showed that the LWIR-based data predicts distortion before catastrophic failure occurs [55].

Unlike visible or NIR cameras, which tend to capture either morphology or high-temperature hot spots with narrow spatial or temporal response, the LWIR modality offers a diffuse, integrated view of temperature distribution across a wide field of view. LWIR sensors operate in the 8–14 µm spectral range, which more closely aligns with the peak blackbody emission of metals at LPBF processing temperatures. Compared to visible or NIR cameras, LWIR imaging is less sensitive to surface reflectivity and more capable of capturing spatially diffuse thermal signals. This allows LWIR sensors to detect broad-area heat retention, post-melt cooling patterns, and subsurface thermal accumulation, making them well suited for layer-resolved thermal mapping in complex geometries. Therefore, LWIRs were also chosen to be investigated under the AMMT program; specifically, a FLIR Boson camera module was selected for this work. The Boson system used was capable of capturing frames up to 60 Hz, with a user-selectable run time mode at 30 Hz. A comparison of the LWIR with the other camera modalities described in this report is shown in Table 2.

Table 2. Summary of the different imaging techniques used under this investigation for the AMMT program, including the new addition of the LWIR cameras

Camera type	Spectral range	Frame rate	Primary function	Integration level
Visible	~400–700 nm	1–5 fps (snapshots)	Surface morphology, powder coverage	Integrated in Peregrine
NIR	~0.9–1.7 µm	~5 fps (video)	Thermal emission	Integrated in Peregrine
Fringe projector	520 nm (green)	2 frames per layer	Surface height reconstruction	Standalone + Peregrine adapter
LWIR	8–14 µm	30–60 fps	Broad thermal field, heat retention	Early-stage deployment + Peregrine integration

Figure 22 shows a summary of the LWIR system's capabilities. The images in Figure 18(a) were collected during a demonstration of a single FLIR Boson camera deployed on a Renishaw AM250. This test was part of a calibration build designed to intentionally induce surface anomalies, including localized overhangs, voids, and residual heat zones. The camera was triggered to capture frames immediately after the laser melting process and again after powder recoating. The postmelt image clearly resolves a variety of high-emissivity regions, with elevated signal intensity corresponding to areas of heat retention, part complexity, and potential lack of fusion. After the recoater pass, these same features remain visible, albeit with lower contrast, suggesting that the LWIR system is not only responsive to transient thermal energy but also to spatial variation in part geometry, surface emissivity, and powder layer coverage. This persistence of thermal features after recoating reinforces LWIR's sensitivity to subsurface and residual heat distribution; this is something that is often lost in visible and NIR imaging. Moreover, some features such as circular voids, sloped ramps, and stepped transitions exhibit thermal signatures even in the postrecoat image, highlighting the potential of LWIR imaging to detect defects through partially obscured powder layers.

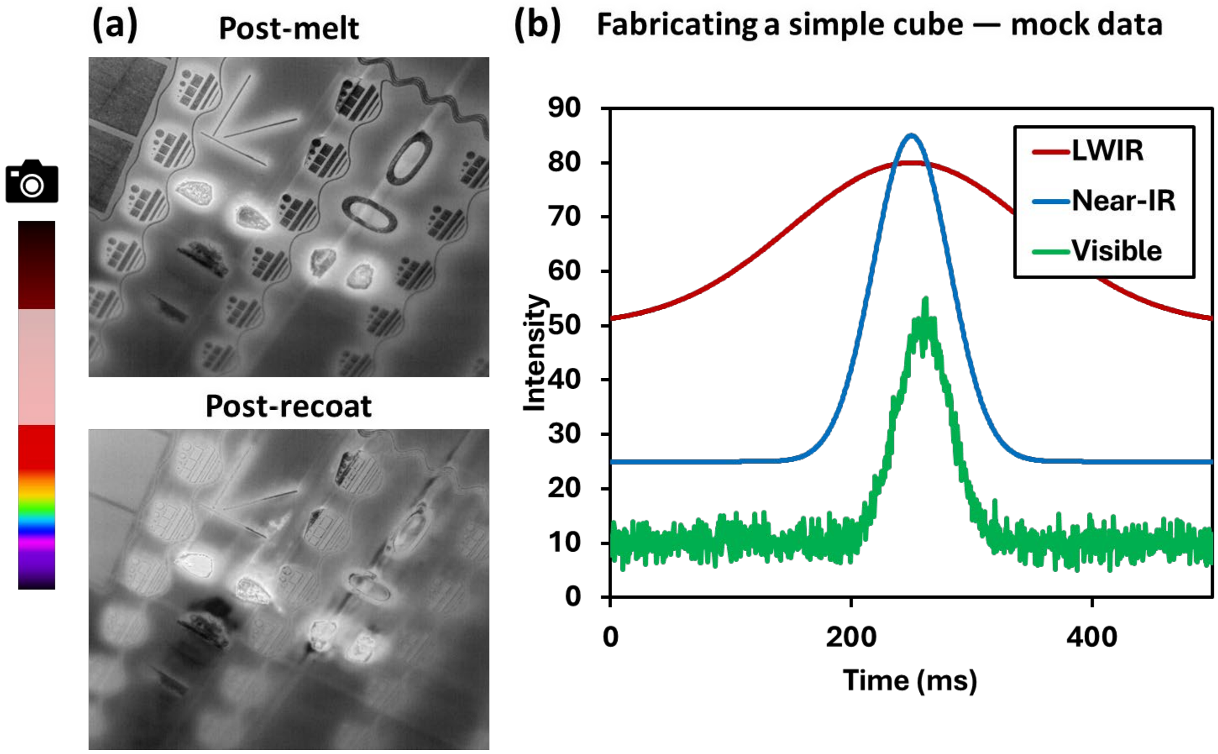

Figure 22. (a) Example images taken from a single LWIR camera deployed in AM250 during a calibration build postmelt and postrecoating. As opposed to the visible or NIR cameras, the spectrum of the LWIR is much broader (8–14 µm). (b) A generalized intensity spectrum from visible, NIR, or LWIR based on laser melting of a single layer of the cube, drawn in Python v3.13.

Figure 22(b) presents simulated data illustrating the differing spatial and spectral responses between LWIR and NIR imaging during the fabrication of a simple cubic geometry. These curves were drawn based on typical spectrums observed in the literature and are not collected data. However, these curves highlight the distinction between modalities in their capture of thermal behavior: LWIR provides an integrated view of heat conduction and accumulation throughout the part, and NIR is sharply focused on capturing real-time laser–material interaction. The normalized intensity profile plotted beneath the images in Figure 22(b) more quantitatively demonstrates the intensity difference of the different camera modalities based on melting of a single layer followed by cooling to room temperature. The LWIR trace (red) displays a broad, smooth curve representative of long-wavelength radiative heat that diffuses across a larger region of the build. The NIR signal (blue) is sharply peaked, consistent with rapid emission from the high-temperature melt pool. Meanwhile, the visible signal (green) is noisier and more sensitive to surface reflectivity and texture rather than thermal state. This spectral comparison supports the conclusion that LWIR imaging is more suitable for assessing global thermal trends and postmelt heat retention, whereas NIR is optimized for transient, localized melt pool monitoring. These differences reinforce the value of integrating multiwavelength imaging approaches for comprehensive thermal process monitoring in LPBF.

5.2 DEPLOYMENT STRATEGY ON RENISHAW AM400

The Renishaw AM400, mentioned earlier in reference to the calibration build shown in Figure 14, was chosen for long-term installation of LWIR cameras using the same Boson camera type that was demonstrated on the AM250, as shown in Figure 22(a). The low resolution of the Boson cameras relative to the size of the AM400's build chamber necessitated locating four cameras ostensibly over the four quadrants of the build plate. Figure 23 shows for the current mounting design of the four Boson cameras within the AM400's build chamber without having to remove the currently mounted visible + NIR cameras.

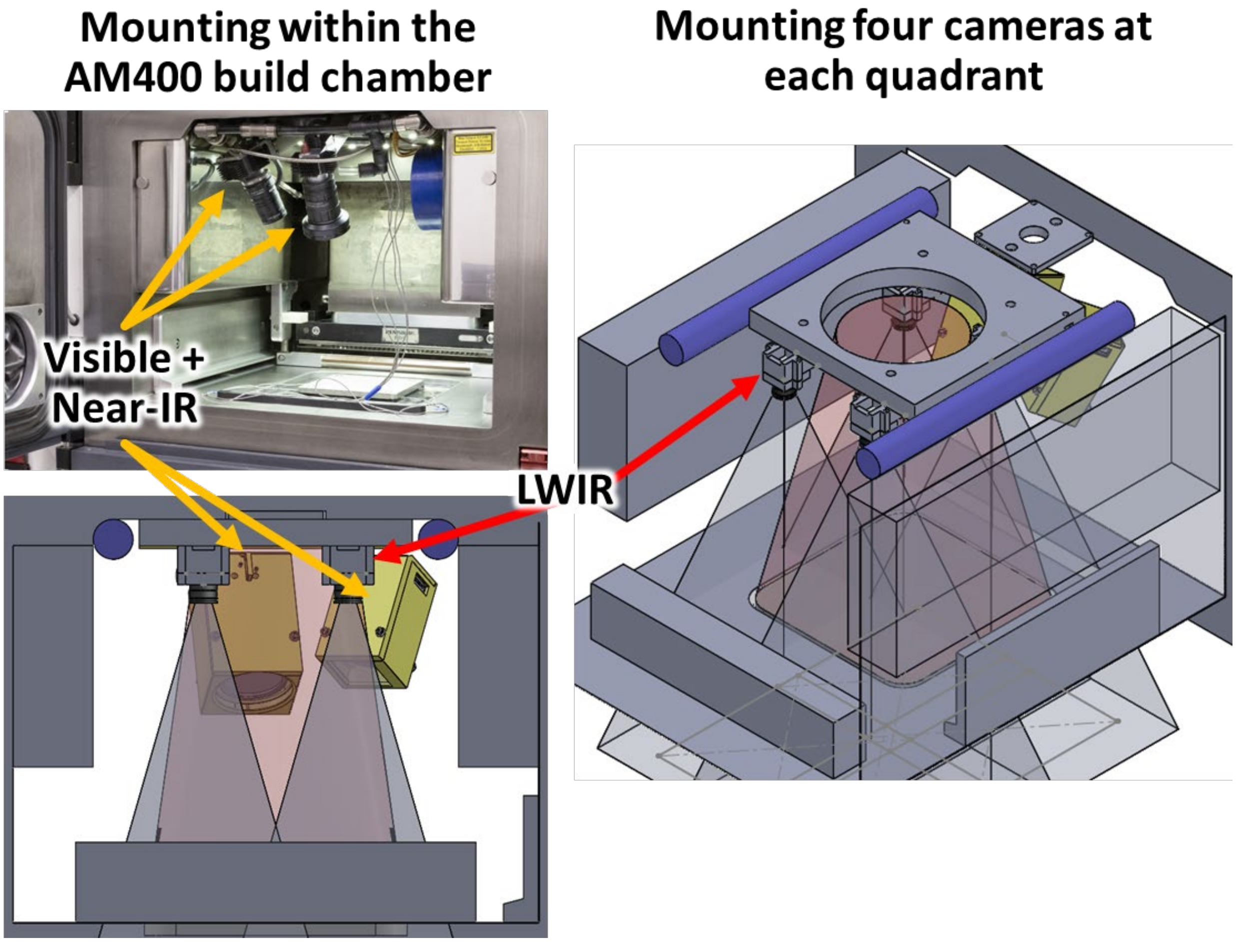

Figure 23. Design for deployment of four Boson LWIR cameras in the build chamber of the AM400, along with the currently installed visible + NIR cameras.

To overcome the limited field of view of a single LWIR camera and enable full coverage of the AM400 build plate, a four-camera stitching approach is currently under development. Each camera is positioned at a quadrant of the build chamber and calibrated to monitor an overlapping section of the plate, enabling image fusion into a single, continuous thermal map. This strategy maximizes spatial resolution and preserves the frame rate and thermal fidelity of each individual sensor. Although a single Boson camera can capture fine thermal gradients, its native field of view (2θ ≈ 50°–95° depending on lens) and small sensor view is insufficient to span the full 250 × 250 mm build area at high resolution. As such, multicamera stitching provides a scalable path toward build-wide LWIR imaging without sacrificing pixel density.

Figure 24(a) demonstrates successful image stitching using Peregrine's internal stitching algorithm, which can align overlapping image frames based on shared pixel content. The example shown here uses high-contrast printed features for alignment, and a resulting composite is formed with minimal seam artifacts. Figure 24(b) shows the mounted LWIR cameras in the AM400 build chamber relative to the visible + NIR cameras. Color-coded overlays highlight the approximate image overlap zones needed to support continuous coverage, and the central red dot marks the geometric center of the build plate. The success of this stitching strategy will enable layer-wise generation of complete thermal maps, which can be used for comparative analysis across zones, early defect localization, and fusion with visible or fringe projection data in future process monitoring efforts.

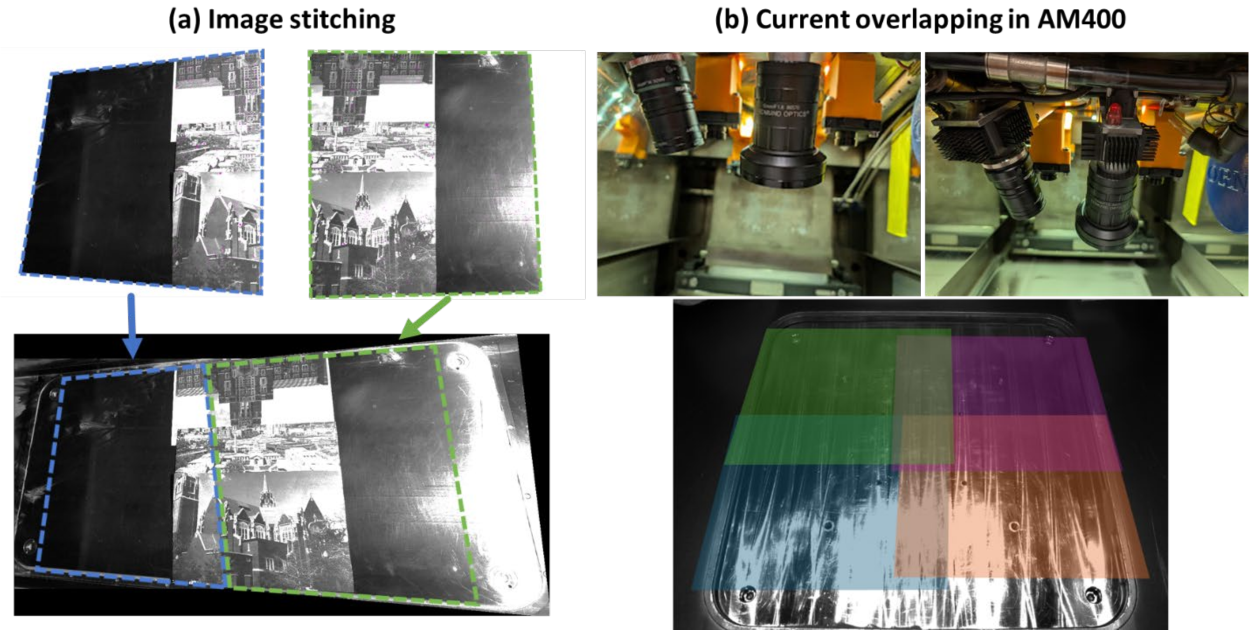

Figure 24. (a) Demonstration of image stitching within Peregrine given enough of an image overlap. (b) Positioning of the four LWIR cameras (orange mounts) relative to the visible + NIR cameras, and the rough overlapping of the current mounting setup for the Boson cameras inside of the AM400's build chamber.

To support robust image stitching and ensure spatial alignment across all four Boson cameras, a calibration procedure is being implemented using physical targets and controlled thermal patterns. A checkerboard pattern mounted to the build plate serves as the primary spatial reference. Each camera captures images of the heated checkerboard under known geometric conditions, and the resulting images are used to solve for lens distortion corrections and other camera intrinsics. Heating the build plate before image acquisition enhances thermal contrast at the checkerboard boundaries, which improves edge detection and corner fitting during calibration. The overlap zones between adjacent cameras are intentionally designed to contain shared features, allowing for pair alignment and stitching refinement. This approach enables pixel-level registration across the full composite image, which is critical for quantitative analysis of thermal gradients, temporal heat flow, and multilayer anomaly detection. Future efforts may incorporate embedded fiducial markers or AM reference geometries to further improve calibration consistency across builds.

Although full integration of LWIR data into Peregrine has not yet been completed as of this reporting, installation of all four Boson cameras is expected to be finalized by the end of FY 2025, and the Peregrine workspace is being prepared to accommodate the new data streams. Future work will explore direct comparisons between the LWIR modality and existing visible + NIR imaging, with particular emphasis on identifying process anomalies and classifying critical anomaly types. A more complex, composite thermal image—formed through stitching and multiwavelength fusion—could provide a richer feature space for anomaly detection algorithms. Fusing LWIR data with NIR and visible channels may be especially valuable for training machine learning algorithms to detect latent thermal drift, build distortion, or part-scale overheating events. Initial results suggest that the LWIR signal offers a more stable and diffuse representation of postmelt thermal behavior, making it well-suited for cross-build comparisons and material–system independent monitoring. As such, LWIR imaging is expected to play a complementary role in multimodal, in situ monitoring frameworks moving forward.

6. INVESTIGATING THERMAL EMMISION SENSING

Figure 25 highlights the relationship between thermal history, VED, and microstructure formation in LPBF, and how this thermal behavior may be captured within a voxel or supervoxel in Peregrine. Variations in cooling rate directly influence the solidification kinetics related to grain/sub-grain growth or solute element distribution kinetics. In LPBF, where heat conduction is highly localized, even small differences in VED or part geometry can cause significant changes in local solidification behavior. Figure 25(a) shows backscatter electron micrographs of melt pools from LPBF-processed SS316L, comparing builds fabricated at high and low VEDs. The differences in melt pool size and subgrain cellular morphology are pronounced, with high VED promoting larger, more columnar structures, and low VED producing finer, more refined features. These microstructural changes are directly tied to cooling rates, which in turn are driven by the rate at which energy is delivered and dissipated during melting; the size and morphology of the melt pool is one indication of the variance in energy densities with respect to the melting and solidification of the powder bed.

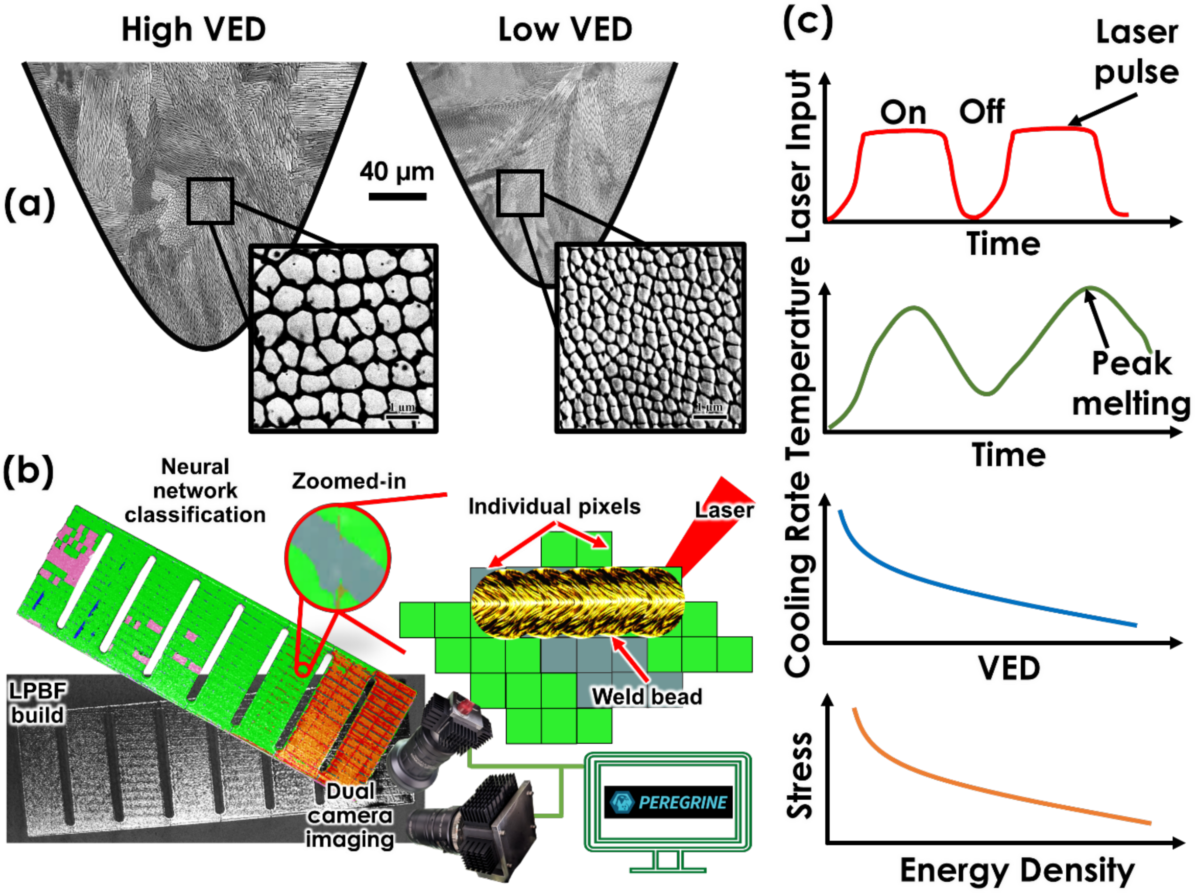

Figure 25. (a) Backscatter electron images of melt pools taken from LPBF processed SS316L fabricated at low and high energy density. Insets from the melt pool show significant variations in the size of the subgrain cellular structure. (b) Zooming into the pixel resolution of Peregrine (~83 µm) compared with the size of the melt pool. (c) Generalized curves for the on/off laser pulsing of the Renishaw AM400's

laser during melting, the corresponding temperature profile in between pulses, and the associated cooling rates and residual stress as a function of VED.

Figure 25(b) compares the typical melt pool dimensions (~200–300 µm wide) to the pixel resolution of Peregrine (~83 µm). This illustrates that even relatively coarse-resolution cameras can capture meaningful thermal and spatial information, as each melt pool spans 2–5 pixels, depending on orientation and process parameters. As such, Peregrine anomaly maps preserve critical information about thermal history within individual voxels or supervoxels, which can be used as input features for downstream models such as VPPM.

Figure 25(c) schematically illustrates how the laser pulsing behavior of the Renishaw AM400 (top), the resulting local temperature evolution (middle), and the cooling rate (bottom) are each a function of VED. As the energy density is increased, the peak melt pool temperature rises, but the cooling rate slows due to longer dwell times and higher heat accumulation (i.e., takes longer for heat to conduct away into the bulk). These observations motivate the need for higher-fidelity, time-resolved thermal sensing. If predictive models are to capture localized defect likelihood or material property changes, then thermal emission signals, particularly those sensitive to cooling rate and melt pool behavior, must be quantified with greater temporal and spectral resolution.

Figure 26 illustrates how high-speed thermal emission data from a photodiode can improve anomaly detection and process understanding compared to standard NIR imaging. In Figure 26(a), Peregrine's layer-wise anomaly segmentation based on visible + NIR imagery (left) is compared against layer-wise thermal intensity maps generated from a photodiode signal (right), overlaid on the component layout. These results are from the calibration build shown in Figure 14 that was fabricated on the M2 system.

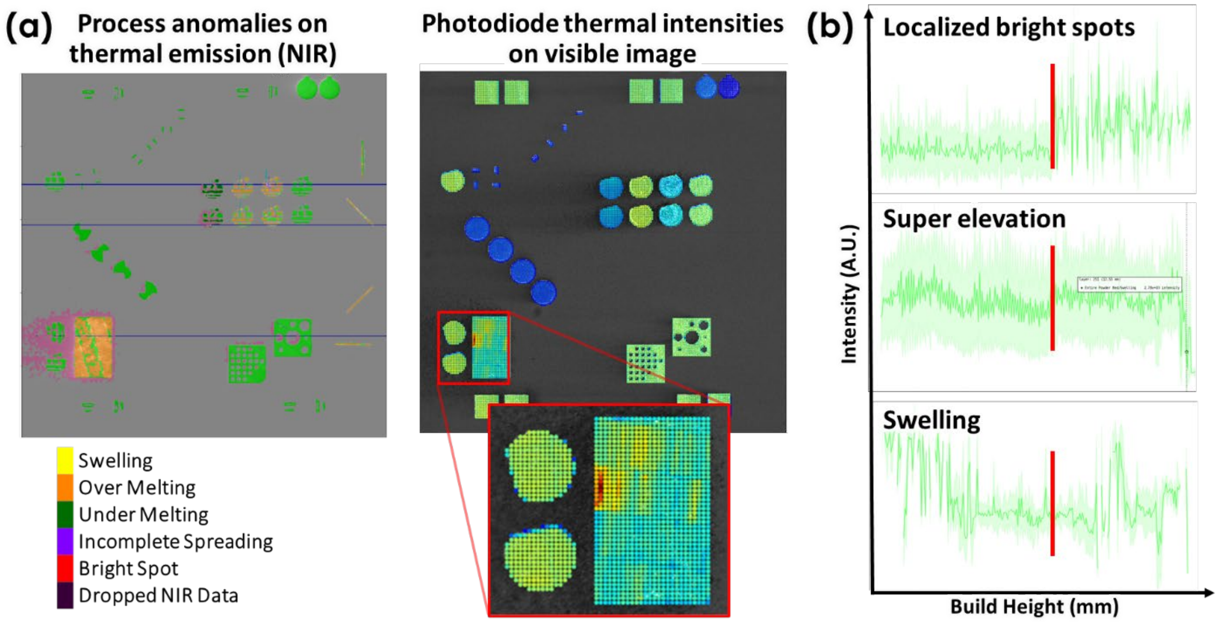

Figure 26. (a) Comparison of intensity spectrums between the thermal emission collected from the NIR camera and a photodiode for the calibration build shown in Figure 14 printed on the M2. (b) Layer-wise (build height) changes in intensity, showing correlations between a sharp increase in bright hot spots with superelevation and swelling.

The photodiode captures a continuous, integrated thermal emission signal during each layer. When mapped to the build coordinate system, localized hot spots appear in regions later identified as having superelevation, swelling, or surface disruptions. A zoom-in on one of the most defect-prone areas (inset) shows that the pixel-wise thermal emission structure is highly heterogeneous—even within single components—suggesting strong spatial correlation between thermal input and later-developing geometry anomalies.

Figure 26(b) shows representative photodiode intensity traces plotted as a function of build height (i.e., layer number) for three regions of interest. In each case, sharp increases in thermal intensity correspond to anomalies previously flagged by Peregrine, including: (1) localized bright spots, indicating elevated energy accumulation or melt pool expansion; (2) superelevation, where the surface rises above the intended build plane; and (3) swelling, often a precursor to delamination or recoater interference. While the photodiode lacks spatial resolution, its high sampling rate and sensitivity to thermal transients make it a valuable complement to camera-based systems. These results suggest that integrating time-resolved thermal emission data can improve anomaly classification and lay the groundwork for feature extraction in machine learning pipelines.

Figure 27 highlights the implementation of a custom-built two-color pyrometry system designed to extract time-resolved thermal emission data during LPBF. As shown in Figure 27(a), a broadband spectrum emitted from the melt pool is collected through a series of collimating and focusing optics and split via a dichroic mirror into two wavelength regimes: 1100–1450 nm and 1500–2000 nm. Edgepass filters remove overlapping wavelengths and isolate the two spectral bands, which are directed to separate photodetectors. The system operates using free-space optics and was mounted externally to the Renishaw AM400 platform. Its optical path includes a fiber-coupled lens stack to enable flexible alignment and narrow spatial targeting within the build chamber.

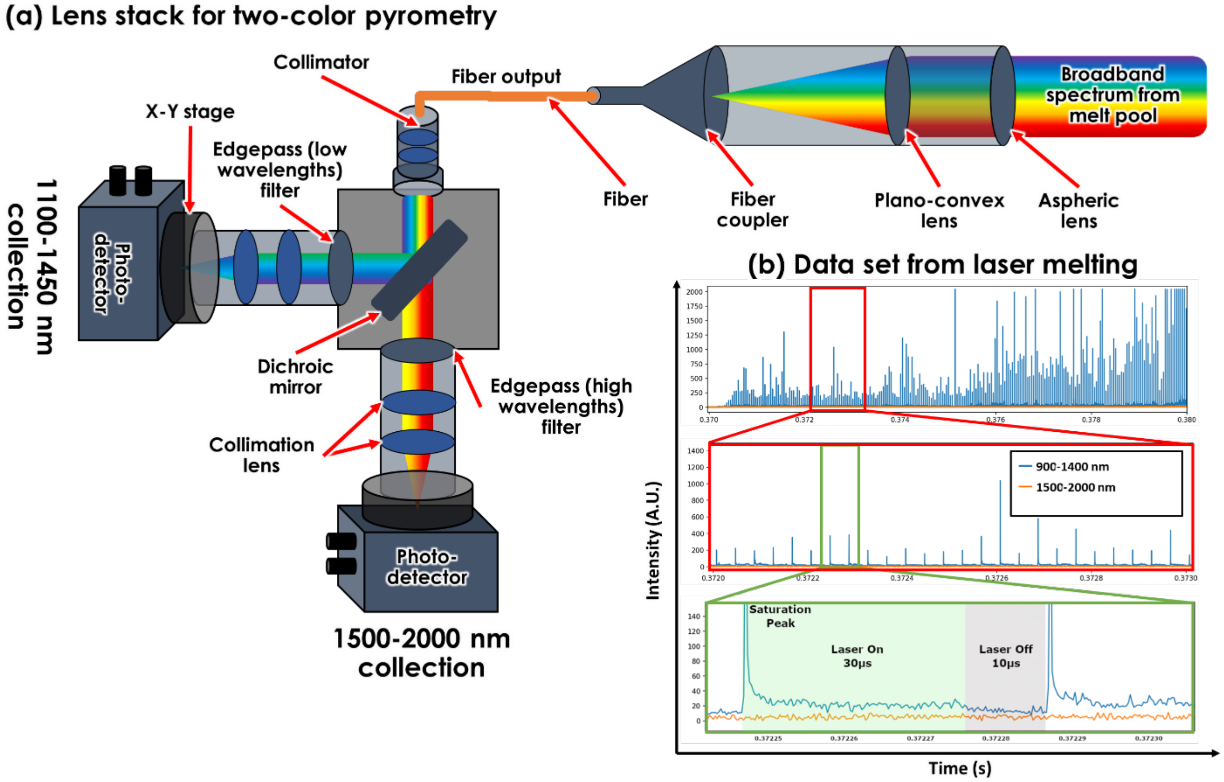

Figure 27. (a) Using free-space optics to design and build a two-color pyrometer that is able to filter out the wavelength of the laser, collimate light, and split the collected broadband spectrum into two sets of low-/high-

wavelength regimes. (b) Data collection from laser melting in a Renishaw AM400, indicating the ability to capture the cooling curve during the off-time of pulsing laser, as discussed in Figure 25(c)

The two-color pyrometer was used to capture thermal emission data during laser melting of LPBF builds fabricated at different energy densities. Figure 27(b) presents sample data from a single melt event, where the top panel shows the full spectrum of raw signal intensity over time. A zoomed-in segment (middle) separates the two wavelength bands, enabling direct comparison of emission trends in the 900–1400 nm and 1500–2000 nm ranges. The bottom panel overlays these data and highlights three important time windows: (1) a short saturation spike corresponding to laser turn-on, (2) a ~30 µs dwell period with laser on, and (3) a ~10 µs cooling period following laser off. Notably, the pyrometer resolves the initial thermal decay curve, a feature that NIR cameras and single-channel photodiodes could not fully capture.

By comparing intensity ratios between the two spectral bands, this system enables temperature estimation independent of emissivity—a significant advantage in dynamic AM environments. Moreover, the ability to track sub-millisecond cooling behavior opens a path to estimating cooling rates, which directly influence microstructure formation, residual stress, and local mechanical properties. These results demonstrate that two-color pyrometry offers a pathway to extract critical thermal data needed for predictive process modeling and future VPPM training. In future efforts, this system will be further integrated into multi-sensor workflows, enabling fusion of spatial, temporal, and spectral data to support component-level qualification.

7. SUMMARY AND FUTURE OUTLOOK

This report documents the deployment and evaluation of in situ monitoring technologies across multiple LPBF platforms under the AMMT program. The focus of this work was to assess the performance of various sensor types in detecting process anomalies that occur under a range of processing conditions, including variations in VED to vary the total energy input into the system.

Several sensor modalities were implemented, including dual visible + NIR cameras, fringe projection profilometry, long-wave infrared (LWIR) thermography, and photodiode and pyrometry systems. These sensors were deployed on LPBF platforms relevant to AMMT, specifically the Concept Laser M2 and Renishaw AM400/AM250 machines. Sensor data were integrated through the Peregrine software platform, which enables spatially resolved classification of anomalies such as recoater streaking, superelevation, swelling, and spatter accumulation.

Calibration builds were used to test how these sensors respond to a range of geometric features and processing parameters. Geometry sets were designed to include unsupported overhangs, thin walls, and angled features that are known to challenge process stability. VED was varied across builds to probe how changes in thermal input affect melt pool behavior and anomaly development. Anomalies detected by Peregrine were found to shift in type and frequency depending on processing conditions, and their spatial distributions were mapped across multiple build layers.

In the case of the thermal emission sensors, NIR imaging provided spatial coverage but limited temporal resolution, while photodiodes and pyrometry systems captured transient thermal signals more effectively. The two-color pyrometer system, in particular, enabled resolution of cooling curves between laser pulses, which are not accessible using camera-based methods.

The techniques and data presented in this report support the milestone objective of identifying limiting process parameter and geometry combinations through in situ monitoring. Looking ahead, future work will focus on integrating these data streams into predictive models, including the Voxel Property

Prediction Model (VPPM). This framework is intended to associate localized in situ data with measured mechanical properties or flaw distributions.

Figure 28 shows the workflow of the longer-term goal, which is to enable prediction-based component qualification by establishing spatial and temporal links between processing conditions, anomaly types, and performance-relevant outcomes. As demonstrated by Scime et al. [35], sub-size specimens can be extracted from various geometries printed in a single build. 100s to 1000s of tensile tests can be performed to assess mechanical behavior, and the data fed back into the VPPM. Ideally, the VPPM would be able to predict the mechanical behavior at site-specific locations; if a hot spot in which Peregrine identifies a process anomaly, it could indicate in real-time (or at least during post-build analysis) whether any limiting flaws impacted the components structural integrity. These efforts contribute to establishing a foundation for a *born-qualified* approach, in which real-time monitoring, anomaly tracking, and predictive modeling together support qualification decisions based on observed process conditions. While this report focuses on the deployment and evaluation of sensor systems, our goal is to demonstrate that collected data in-situ will inform future predictive frameworks that aim to reduce reliance on destructive testing and shorten qualification timelines.

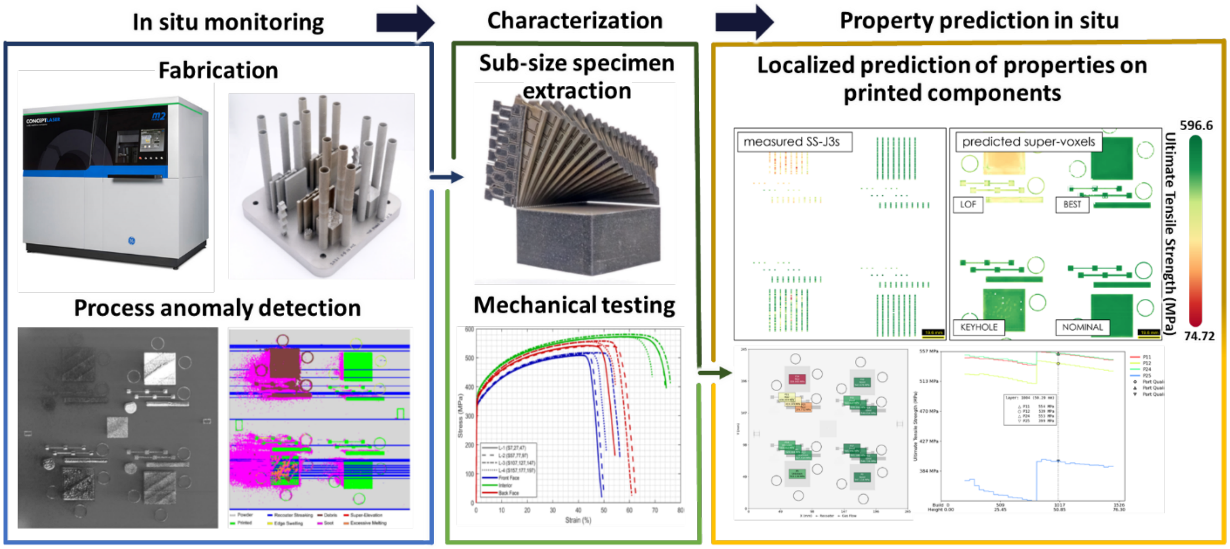

Figure 28. General process flow for moving toward prediction-based modeling inside Peregrine. Scime et al. [35] demonstrated the ability to read in thousands of tensile curves from extracted SS3 subspecimens of a build into Peregrine and predict site-specific mechanical properties based on detected anomalies.

8. REFERENCES

[1] G.S. Was, D. Petti, S. Ukai, S. Zinkle, Materials for future nuclear energy systems, Journal of Nuclear Materials 527 (2019) 151837.
[2] S.J. Zinkle, K.A. Terrani, L.L. Snead, Motivation for utilizing new high-performance advanced materials in nuclear energy systems, Current Opinion in Solid State and Materials Science 20(6) (2016) 401-410.
[3] S.J. Zinkle, G.S. Was, Materials challenges in nuclear energy, Acta Materialia 61(3) (2013) 735-758.
[4] R.N. Wright, Updated draft ASME boiler and pressure vessel code case for use of Alloy 617 for construction of nuclear components for section III division 5, Idaho National Lab.(INL), Idaho Falls, ID (United States), 2018.
[5] T.-L. Sham, R.E. Bass, Y. Wang, X. Zhang, A709 Qualification Plan Update and Mechanical Properties Data Assessment, Idaho National Lab.(INL), Idaho Falls, ID (United States), 2022.

[6] T.-L. Sham, K. Natesan, Code qualification plan for an advanced austenitic stainless steel, alloy 709, for sodium fast reactor structural applications, (2017).
[7] S. Cetiner, P. Ramuhalli, Transformational Challenge Reactor Autonomous Control System Framework and Key Enabling Technologies, United States, 2019, p. Medium: ED.
[8] B. Betzler, B. Ade, A. Wysocki, P. Jain, P. Chesser, M. Greenwood, K. Terrani, Transformational Challenge Reactor preconceptual core design studies, Nuclear Engineering and Design 367 (2020) 110781.
[9] B.R. Betzler, B.J. Ade, P.K. Jain, A.J. Wysocki, P.C. Chesser, W.M. Kirkland, M.S. Cetiner, A. Bergeron, F. Heidet, K.A. Terrani, Conceptual Design of the Transformational Challenge Reactor, Nuclear Science and Engineering (2022) 1-26.
[10] Z. Gan, O.L. Kafka, N. Parab, C. Zhao, L. Fang, O. Heinonen, T. Sun, W.K. Liu, Universal scaling laws of keyhole stability and porosity in 3D printing of metals, Nature Communications 12(1) (2021) 2379.
[11] B. Ade, B. Betzler, A. Wysocki, J. Weinmeister, N. See, P. Jain, W. Kirkland, J. Burns, B. Hiscox, D. Schappel, A. Talamo, A. Bergeron, C.J. Jessee, Transformational Challenge Reactor Design Characteristics, Conference: PHYSOR 2022: International Conference on Physics of Reactors 2022 - Oak Ridge, Tennessee, United States of America - 5/15/2022 8:00:00 AM-5/20/2022 8:00:00 AM, United States, 2022, p. Medium: ED.
[12] B.R. Betzler, B.J. Ade, A. Wysocki, P. Chesser, M.S. Greenwood, P. Wang, N. See, X. Hu, K. Terrani, Design Downselection for the Transformational Challenge Reactor, Oak Ridge National Lab. (ORNL), Oak Ridge, TN (United States), 2020.
[13] B.R. Betzler, B.J. Ade, A.J. Wysocki, P.K. Jain, P.C. Chesser, M.S. Greenwood, K.A. Terrani, Transformational Challenge Reactor preconceptual core design studies, Nucl. Eng. Des. 367 (2020) 110781.
[14] M. Li, R.R. Dehoff, A.M. Jokisaari, M.D. McMurtrey, I.J.V. Rooyen, D. Cairns-Gallimore, Department of Energy Office of Nuclear Energy Advanced Materials and Manufacturing Technologies (AMMT) 2025 Roadmap, Argonne National Laboratory, 2025.
[15] W.J. Sames, F. List, S. Pannala, R.R. Dehoff, S.S. Babu, The metallurgy and processing science of metal additive manufacturing, International Materials Reviews 61(5) (2016) 315-360.
[16] H.C. Hyer, C.M. Petrie, Effect of powder layer thickness on the microstructural development of additively manufactured SS316, Journal of Manufacturing Processes 76 (2022) 666-674.
[17] H. Hyer, L. Zhou, S. Park, G. Gottsfritz, G. Benson, B. Tolentino, B. McWilliams, K. Cho, Y. Sohn, Understanding the Laser Powder Bed Fusion of AlSi10Mg Alloy, Metallography, Microstructure, and Analysis 9 (2020) 484-502.
[18] M. Rolchigo, J. Coleman, G.L. Knapp, A. Plotkowski, Grain structure and texture selection regimes in metal powder bed fusion, Additive Manufacturing 81 (2024) 104024.
[19] T. Voisin, J.-B. Forien, A. Perron, S. Aubry, N. Bertin, A. Samanta, A. Baker, Y.M. Wang, New insights on cellular structures strengthening mechanisms and thermal stability of an austenitic stainless steel fabricated by laser powder-bed-fusion, Acta Materialia 203 (2021) 116476.
[20] K. Huang, C. Kain, N. Diaz-Vallejo, Y. Sohn, L. Zhou, High throughput mechanical testing platform and application in metal additive manufacturing and process optimization, Journal of Manufacturing Processes 66 (2021) 494-505.
[21] S. Dryepondt, P. Nandwana, P. Fernandez-Zelaia, F. List, Microstructure and high temperature tensile properties of 316L fabricated by laser powder-bed fusion, Additive Manufacturing 37 (2021) 101723.
[22] M. Messner, B. Barua, A. Huning, S. Arndt, C. Massey, S. Taller, R. Dehoff, M. Russell, L. Scime, Z. Snow, ASME Code Qualification Plan for LPBF 316 SS, Argonne National Laboratory (ANL), Argonne, IL (United States), 2023.
[23] C. Massey, P. Nandwana, H. Hyer, S. Nayir, J. Kendall, C. Joslin, R. Duncan, D. Collins, T. Graening Seibert, F. List III, L. Scime, Z. Snow, A. Ziabari, T. Butcher, R. Dehoff, Data-Driven

Optimization of the Processing Window for 316H Components Fabricated Using Laser Powder Bed Fusion, Oak Ridge National Laboratory, ak Ridge National Laboratory, 2023.
[24] C. Massey, P. Nandwana, H. Hyer, S. Nayir, G. Kumari, J. Kendall, C. Joslin, D. Collins, T. Graening, A. Godfrey, A.M. Rossy, A. Ziabari, Process–Property–Performance Mapping of Additively Manufactured 316H Stainless Steel Components, Oak Ridge National Laboratory, 2024.
[25] P. Nandwana, R. Kannan, S. Nayir, C. Massey, C. Joslin, F. List III, Preliminary Report on Compositional Specification for Printed 316SS, Oak Ridge National Laboratory (ORNL), Oak Ridge, TN (United States), 2023.
[26] H. Hyer, R. Newell, D. Matejczyk, S. Hsie, M. Anthony, L. Zhou, C. Kammerer, Y. Sohn, Microstructural Development in As Built and Heat Treated IN625 Component Additively Manufactured by Laser Powder Bed Fusion, Journal of Phase Equilibria and Diffusion (2021).
[27] J.L. Bartlett, X. Li, An overview of residual stresses in metal powder bed fusion, Additive Manufacturing 27 (2019) 131-149.
[28] Y. AbouelNour, N. Gupta, In-situ monitoring of sub-surface and internal defects in additive manufacturing: A review, Materials & Design (2022) 111063.
[29] L. Scime, J. Beuth, Anomaly detection and classification in a laser powder bed additive manufacturing process using a trained computer vision algorithm, Additive Manufacturing 19 (2018) 114-126.
[30] L. Scime, B. Fisher, J. Beuth, Using coordinate transforms to improve the utility of a fixed field of view high speed camera for additive manufacturing applications, Manufacturing Letters 15 (2018) 104-106.
[31] L. Scime, D. Siddel, S. Baird, V. Paquit, Layer-wise anomaly detection and classification for powder bed additive manufacturing processes: A machine-agnostic algorithm for real-time pixel-wise semantic segmentation, Additive Manufacturing 36 (2020) 101453.
[32] L. Scime, A. Singh, V. Paquit, A scalable digital platform for the use of digital twins in additive manufacturing, Manufacturing Letters 31 (2022) 28-32.
[33] Z. Snow, L. Scime, A. Ziabari, B. Fisher, V. Paquit, Observation of spatter-induced stochastic lack-of-fusion in laser powder bed fusion using in situ process monitoring, Additive Manufacturing 61 (2023) 103298.
[34] L. Scime, J. Beuth, Using machine learning to identify in-situ melt pool signatures indicative of flaw formation in a laser powder bed fusion additive manufacturing process, Additive Manufacturing 25 (2019) 151-165.
[35] L. Scime, C. Joslin, D.A. Collins, M. Sprayberry, A. Singh, W. Halsey, R. Duncan, Z. Snow, R. Dehoff, V. Paquit, A Data-Driven Framework for Direct Local Tensile Property Prediction of Laser Powder Bed Fusion Parts, Materials 16(23) (2023) 7293.
[36] M. Schreiber, J.A. Ramirez, G. Hommer, Y. Jin, C. Smith, J. Klemm-Toole, C. Brice, J. Gockel, Rationalizing Different Microstructures and Yield Strengths of Cross-Platform Laser Powder Bed Fusion 316L, Metallurgical and Materials Transactions A (2025).
[37] J. Liu, P. Wen, Metal vaporization and its influence during laser powder bed fusion process, Materials & Design 215 (2022) 110505.
[38] A.J. Dunbar, E.R. Denlinger, M.F. Gouge, T.W. Simpson, P. Michaleris, Comparisons of laser powder bed fusion additive manufacturing builds through experimental in situ distortion and temperature measurements, Additive Manufacturing 15 (2017) 57-65.
[39] C.M. Petrie, N. Sridharan, In situ measurement of phase transformations and residual stress evolution during welding using spatially distributed fiber-optic strain sensors, Measurement Science and Technology 31(12) (2020) 125602.
[40] H.-H. König, N.H. Pettersson, A. Durga, S. Van Petegem, D. Grolimund, A.C. Chuang, Q. Guo, L. Chen, C. Oikonomou, F. Zhang, G. Lindwall, Solidification modes during additive manufacturing of steel revealed by high-speed X-ray diffraction, Acta Materialia 246 (2023) 118713.

[41] C. Zhao, K. Fezzaa, R.W. Cunningham, H. Wen, F. De Carlo, L. Chen, A.D. Rollett, T. Sun, Real-time monitoring of laser powder bed fusion process using high-speed X-ray imaging and diffraction, Scientific Reports 7(1) (2017).
[42] C. Zhao, N.D. Parab, X. Li, K. Fezzaa, W. Tan, A.D. Rollett, T. Sun, Critical instability at moving keyhole tip generates porosity in laser melting, Science 370(6520) (2020) 1080-1086.
[43] A. Ziabari, S.V. Venkatakrishnan, Z. Snow, A. Lisovich, M. Sprayberry, P. Brackman, C. Frederick, P. Bhattad, S. Graham, P. Bingham, R. Dehoff, A. Plotkowski, V. Paquit, Enabling rapid X-ray CT characterisation for additive manufacturing using CAD models and deep learning-based reconstruction, npj Computational Materials 9(1) (2023) 91.
[44] R. McCann, M.A. Obeidi, C. Hughes, É. McCarthy, D.S. Egan, R.K. Vijayaraghavan, A.M. Joshi, V.A. Garzon, D.P. Dowling, P.J. McNally, In-situ sensing, process monitoring and machine control in Laser Powder Bed Fusion: A review, Additive Manufacturing 45 (2021) 102058.
[45] Y. Ma, Y. Yin, S. Jiang, X. Li, F. Huang, B. Sun, Single pixel 3D imaging with phase-shifting fringe projection, Optics and Lasers in Engineering 140 (2021) 106532.
[46] Z. Cai, X. Liu, A. Li, Q. Tang, X. Peng, B.Z. Gao, Phase-3D mapping method developed from back-projection stereovision model for fringe projection profilometry, Optics express 25(2) (2017) 1262-1277.
[47] J. Wang, Z. Zhang, R.K. Leach, W. Lu, J. Xu, Predistorting projected fringes for high-accuracy 3-D phase mapping in fringe projection profilometry, IEEE Transactions on Instrumentation and Measurement 70 (2021) 1-9.
[48] B. Zhang, K. Jiang, J. Lin, A novel in-situ calibration method based on virtual planes for fringe projection profilometry, IEEE Transactions on Instrumentation and Measurement (2024).
[49] B. Zhang, J. Ziegert, F. Farahi, A. Davies, In situ surface topography of laser powder bed fusion using fringe projection, Additive Manufacturing 12 (2016) 100-107.
[50] R.W. Penny, Z. Kutschke, A.J. Hart, High-fidelity optical monitoring of laser powder bed fusion via aperture division multiplexing, npj Advanced Manufacturing 2(1) (2025) 28.
[51] A. Surana, M.E. Lynch, A.R. Nassar, G.C. Ojard, B.A. Fisher, D. Corbin, R. Overdorff, Flaw detection in multi-laser powder bed fusion using in situ coaxial multi-spectral sensing and deep learning, Journal of Manufacturing Science and Engineering 145(5) (2023) 051005.
[52] L. Scime, M. Sprayberry, D. Collins, A. Singh, C. Joslin, R. Duncan, J. Simpson, F. List III, K. Carver, A. Huning, Diagnostic and Predictive Capabilities of the TCR Digital Platform, (2021).
[53] N. O'Dowd, C.J. Sutcliffe, Structured light part quality monitoring for additive manufacturing and methods of use, Google Patents, 2024.
[54] N. O'Dowd, Inspect Additive Manufacturing, stop monitoring: Phase3D’s unit-based, in-process inspection solution for powder bed AM, Metal AM, 2024.
[55] T. Liu, E.C. Kinzel, M.C. Leu, In-situ lock-in thermographic measurement of powder layer thermal diffusivity and thickness in laser powder bed fusion, Additive Manufacturing 74 (2023) 103726.
[56] M. Reza Yavari, R.J. Williams, K.D. Cole, P.A. Hooper, P. Rao, Thermal Modeling in Metal Additive Manufacturing Using Graph Theory: Experimental Validation With Laser Powder Bed Fusion Using In Situ Infrared Thermography Data, Journal of Manufacturing Science and Engineering 142(12) (2020).